

Scale-Dependent Infrared Radiative Damping Rates on Mars and Their Role in the Deposition of Gravity-Wave Momentum Flux

Stephen D. Eckermann^{a,*}, Jun Ma^b, Xun Zhu^c

^a*Space Science Division, Code 7646, Naval Research Laboratory, 4555 Overlook Avenue SW, Washington, DC 20375, USA*

^b*Computational Physics, Inc., 8001 Braddock Road, Springfield, Virginia 22151, USA*

^c*Johns Hopkins University/Applied Physics Laboratory, 11100 Johns Hopkins Road, Laurel, Maryland 27023, USA*

Abstract

Using a Curtis matrix model of 15 μm CO_2 radiative cooling rates for the Martian atmosphere, we have computed vertical scale-dependent IR radiative damping rates from 0-200 km altitude over a broad band of vertical wavenumbers $m = 2\pi(1\text{--}500 \text{ km})^{-1}$ for representative meteorological conditions at 40°N and average levels of solar activity and dust loading. In the middle atmosphere, infrared (IR) radiative damping rates increase with decreasing vertical scale and peak in excess of 30 days^{-1} at $\sim 50\text{--}80$ km altitude, before gradually transitioning to scale-independent rates above ~ 100 km due to breakdown of local thermodynamic equilibrium. We incorporate these computed IR radiative damping rates into a linear anelastic gravity-wave model to assess the impact of IR radiative damping, relative to wave breaking and molecular viscosity, in the dissipation of gravity-wave momentum flux. The model results indicate that IR radiative damping is the dominant process in dissipating gravity-wave momentum fluxes at $\sim 0\text{--}50$ km altitude, and is the dominant process at all altitudes for gravity waves with vertical wavelengths $\lesssim 10\text{--}15$ km. Wave breaking becomes dominant at higher altitudes only for “fast” waves of short horizontal and long vertical wavelengths. Molecular viscosity plays a negligible role in overall momentum-flux deposition. Our results provide compelling evidence that IR radiative damping is a major, and often dominant physical process controlling the dissipation of gravity wave momentum fluxes on Mars, and therefore should be incorporated into future parameterizations of gravity-wave drag within Mars GCMs. Lookup tables for doing so, based on the current computations, are provided.

Keywords:

Mars (atmosphere), Mars (climate), Atmospheres (dynamics), Radiative transfer, Aeronomy

Report Documentation Page		Form Approved OMB No. 0704-0188
Public reporting burden for the collection of information is estimated to average 1 hour per response, including the time for reviewing instructions, searching existing data sources, gathering and maintaining the data needed, and completing and reviewing the collection of information. Send comments regarding this burden estimate or any other aspect of this collection of information, including suggestions for reducing this burden, to Washington Headquarters Services, Directorate for Information Operations and Reports, 1215 Jefferson Davis Highway, Suite 1204, Arlington VA 22202-4302. Respondents should be aware that notwithstanding any other provision of law, no person shall be subject to a penalty for failing to comply with a collection of information if it does not display a currently valid OMB control number.		
1. REPORT DATE 2010	2. REPORT TYPE	3. DATES COVERED 00-00-2010 to 00-00-2010
4. TITLE AND SUBTITLE Scale-Dependent Infrared Radiative Damping Rates on Mars and Their Role in the Deposition of Gravity-Wave Momentum Flux		5a. CONTRACT NUMBER
		5b. GRANT NUMBER
		5c. PROGRAM ELEMENT NUMBER
6. AUTHOR(S)	5d. PROJECT NUMBER	
	5e. TASK NUMBER	
	5f. WORK UNIT NUMBER	
7. PERFORMING ORGANIZATION NAME(S) AND ADDRESS(ES) Naval Research Laboratory, Space Science Division, Code 7646, 4555 Overlook Avenue SW, Washington, DC, 20375		8. PERFORMING ORGANIZATION REPORT NUMBER
9. SPONSORING/MONITORING AGENCY NAME(S) AND ADDRESS(ES)		10. SPONSOR/MONITOR'S ACRONYM(S)
		11. SPONSOR/MONITOR'S REPORT NUMBER(S)
12. DISTRIBUTION/AVAILABILITY STATEMENT Approved for public release; distribution unlimited		
13. SUPPLEMENTARY NOTES Icarus (submitted).		
14. ABSTRACT Using a Curtis matrix model of 15 m CO₂ radiative cooling rates for the Martian atmosphere, we have computed vertical scale-dependent IR radiative damping rates from 0-200 km altitude over a broad band of vertical wavenumbers $m = 2$ (1?500 km) for representative meteorological conditions at 40°N and average levels of solar activity and dust loading. In the middle atmosphere infrared (IR) radiative damping rates increase with decreasing vertical scale and peak in excess of 30 days at 8764;50?80 km altitude, before gradually transitioning to scale-independent rates above 8764;100 km due to breakdown of local thermodynamic equilibrium. We incorporate these computed IR radiative damping rates into a linear anelastic gravity-wave model to assess the impact of IR radiative damping, relative to wave breaking and molecular viscosity, in the dissipation of gravity-wave momentum flux. The model results indicate that IR radiative damping is the dominant process in dissipating gravity-wave momentum fluxes at 8764;0?50 km altitude, and is the dominant process at all altitudes for gravity waves with vertical wavelengths .10?15 km. Wave breaking becomes dominant at higher altitudes only for fast waves of short horizontal and long vertical wavelengths. Molecular viscosity plays a negligible role in overall momentum-flux deposition. Our results provide compelling evidence that IR radiative damping is a major, and often dominant physical process controlling the dissipation of gravity wave momentum fluxes on Mars and therefore should be incorporated into future parameterizations of gravity-wave drag within Mars GCMs. Lookup tables for doing so, based on the current computations, are provided.		
15. SUBJECT TERMS		

16. SECURITY CLASSIFICATION OF:			17. LIMITATION OF ABSTRACT Same as Report (SAR)	18. NUMBER OF PAGES 40	19a. NAME OF RESPONSIBLE PERSON
a. REPORT unclassified	b. ABSTRACT unclassified	c. THIS PAGE unclassified			

*Corresponding Author: Tel +1(202)404-1299; Fax +1(202)404-8090; E-mail address: `stephen.eckermann@nrl.navy.mil`

Email addresses: `stephen.eckermann@nrl.navy.mil` (Stephen D. Eckermann), `jma@cpi.com` (Jun Ma), `xun.zhu@jhuapl.edu` (Xun Zhu)

Preprint submitted to Icarus

June 3, 2010

1. Introduction

Being $\sim 95\%$ CO_2 by mixing ratio, the thermal balance of the Martian atmosphere is driven to a large degree by infrared (IR) radiative transfer (RT) among CO_2 bands, particularly $15\ \mu\text{m}$ cooling and heating by absorption of solar radiation in near-IR bands. The advent of satellite remote sensing of the Martian atmosphere has spurred development of detailed atmospheric RT codes (López-Valverde and López-Puertas, 1994), to improve both the retrieval of atmospheric parameters from passive IR remote sensors (Kleinböhl et al., 2009), as well as the parameterizations of radiative heating and cooling rates embedded within Martian general circulation models (GCMs: e.g., González-Galindo et al., 2009). These models have highlighted the importance of departures from local thermodynamic equilibrium (LTE) in CO_2 IR RT that significantly modify net heating and cooling rates above ~ 80 km altitude (López-Puertas and López-Valverde, 1995; López-Valverde et al., 1998).

Finite computational resources make it impractical to incorporate detailed RT codes within Martian GCMs to compute net CO_2 IR heating and cooling rates, and much simpler (i.e. faster) parameterizations are needed. CO_2 IR radiative cooling rates are currently parameterized in Mars GCMs at high altitudes by local cooling-to-space approximations tuned to reproduce results of detailed offline non-LTE RT calculations, and at low altitudes by simplified wide-band LTE-based schemes (Forget et al., 1999; Richardson et al., 2007; González-Galindo et al., 2009).

These same computational constraints force the GCMs to operate at gridpoint resolutions that are too coarse to resolve the full spatial spectrum of atmospheric dynamics that can exist in the Martian atmosphere (Imamura et al., 2007). Gravity waves, for example, are mostly unresolved by Martian GCMs, and so the missing effects of their momentum flux deposition on the resolved circulation (so-called gravity-wave drag) must be parameterized, again using simplified fast algorithms (e.g., Joshi et al., 1996; Collins et al., 1997; Forget et al., 1999).

Local IR cooling parameterizations ignore the inherently nonlocal nature of radiative cooling: for example, that an atmospheric layer wedged between two colder layers will generally cool more rapidly than if the temperature is identical in all three layers. Thus vertical structure in atmospheric temperature profiles can significantly change IR cooling rates. At higher altitudes where cooling

rates on Mars are the largest, most of the short vertical scale structure in atmospheric temperature profiles is produced by gravity wave oscillations (Fritts et al., 2006; Creasey et al., 2006), which the GCMs do not resolve. This suggests a potentially important interaction between gravity wave dynamics and IR radiative cooling that the existing uncoupled parameterizations of each process in Mars GCMs miss entirely.

The general issue has been recognized in planetary atmosphere for many years (e.g., Spiegel, 1957; Sasamori and London, 1966; Goody and Belton, 1967). In the Earth’s atmosphere, Fels (1982) showed that standard WKB methods for gravity waves could be applied in the computation of the gravity-wave-modulated IR cooling rate, which yielded a local IR radiative relaxation rate that acted to damp the gravity wave-induced temperature perturbations. This damping rate varied according to the wave’s vertical wavelength λ_z . The Fels approach has been extended in various ways to more realistic non-LTE RT models (Shved and Utyakovsky, 1983; Fels, 1984; Zhu and Strobel, 1991; Zhu, 1993; Bresser et al., 1995) and the resulting scale-dependent IR damping rates have been incorporated within parameterizations of gravity wave dynamics on Earth (e.g., Marks and Eckermann, 1995; Eckermann and Marks, 1997).

The analytical methods of Fels (1984) were applied by Imamura and Ogawa (1995) to 15 μm CO₂ cooling within the atmospheres of Earth, Mars and Venus. On Mars, they inferred scale-dependent IR damping rates that were significantly faster than on Earth. They also estimated the relative impacts of molecular viscosity and radiative cooling on the dissipation of gravity waves as a function of altitude and λ_z on each planet. Despite these suggestive preliminary findings, there has been, as far as we are aware, no additional research on scale-dependent IR radiative damping on Mars. In particular, it continues to be unclear whether IR radiative damping has any relevance to the dissipation of gravity-wave momentum flux on Mars.

Thus, this study has two parts. First, in section 2 we formulate and validate a Curtis-matrix model of 15 μm radiative cooling on Mars, and apply it in section 3 to compute scale-dependent IR radiative damping rates. Then, in section 4 we incorporate these damping rates into simple anelastic models of gravity wave dynamics on Mars, to assess their impact on gravity-wave momentum-flux deposition, relative to wave breaking and molecular viscous dissipation. Section 5 summarizes our major findings and conclusions concerning the impact of IR radiative damping on

gravity-wave momentum-flux deposition on Mars.

2. CO₂ 15 μ m Cooling Rates for Mars

2.1. Model

Exact calculations of CO₂ IR cooling rates involve solving the RT equation numerically using first-principles line-by-line integration through an optically thick Martian atmosphere. High accuracy requires multiple integrations over a range of radiance paths and a fine IR frequency grid, which is prohibitively expensive computationally, and thus performed only occasionally for validation purposes (e.g., Zhu, 1990; Fomichev, 2009). In common with many previous studies of IR cooling on Earth (e.g., Zhu, 1990) and Mars (e.g., López-Valverde and López-Puertas, 1994), we compute a faster approximate solution using Curtis matrices.

Ignoring boundary flux terms, the cooling rate expressed in Curtis-matrix form is

$$\mathbf{Q} \equiv \frac{d\mathbf{T}}{dt} = \mathbf{C}\mathbf{\Theta}. \quad (1)$$

Here \mathbf{Q} , \mathbf{T} and $\mathbf{\Theta}$ are column vectors representing a discretized vertical profile of cooling rate, temperature and normalized source function at a series of vertical grid points $k = 1 \dots L$ at successive altitude (pressure) levels z_k (p_k), and \mathbf{C} is the $L \times L$ Curtis matrix that specifies the generally nonlocal dependence of cooling rate on temperature and mixing ratio.

Inclusion of a complete list of CO₂ vibration-translation (V-T) and vibration-vibration (V-V) transitions in (1) yields a large number of nonlinearly coupled rate and RT equations which can be very difficult or even impractical to solve numerically (Kutepov et al., 1998). For the reduced collection of major V-T and V-V transitions used by Dickinson (1984), Zhu (1990) showed that nonlinearity in the resulting equations arose from coupling terms due to V-V exchanges which, if eliminated, reduced the system to an equivalent two-energy-level problem. While V-V transitions are clearly significant to the RT in individual sub-bands, Zhu (1990) argued that they were less significant in determining total non-LTE cooling rates over the entire band. Offline calculations by Zhu and Strobel (1990) found errors of no more than $\sim 1 \text{ K day}^{-1}$ in total IR cooling rate at the Earth's mesopause when V-V transitions were ignored. For Mars, López-Puertas and López-Valverde (1995) also found little change in total cooling rate when V-V rates were varied. Their

results also indicated that the contribution of V-V transitions to the total cooling rate in the Martian atmosphere is smaller than on Earth. Hence we ignore V-V transitions in what follows.

For the resulting equivalent two-energy-level Curtis-matrix model of Zhu (1990), Zhu et al. (1992) developed an algorithm for deriving cooling rates for arbitrary atmospheres by interpolating a reference Curtis matrix \mathbf{C}_0 , computed for reference profiles of pressure p_0 , temperature T_0 and CO_2 mixing ratio $r_0^{\text{CO}_2}$, to yield a solution for given p , T and r^{CO_2} . The element (j, k) of the interpolated Curtis matrix \mathbf{C} is derived by modifying the reference value C_{jk}^0 as

$$\begin{aligned} C_{jk} = & C_{jk}^0 + A_{jk}^{10} \delta T_j + A_{jk}^{01} \nabla_{jk} + \frac{1}{2} A_{jk}^{20} (\delta T_j)^2 + \frac{1}{2} A_{jk}^{02} (\nabla_{jk})^2 \\ & + A_{jk}^{11} (\delta T_j) (\nabla_{jk}) + \gamma_{jk}^{01} \Pi_{jk} + \frac{1}{2} \gamma_{jk}^{02} (\Pi_{jk})^2. \end{aligned} \quad (2)$$

The matrices $A^{\alpha\beta}$, defined in (24a)-(24e) of Zhu (1990), are differencing approximations of derivatives resulting from Taylor series approximation of the escape function at levels p_j and p_k , and δT_j is a temperature correction from the reference (T_0) to actual temperature T at level p_j . Following Fels and Schwarzkopf (1981), the matrix

$$\nabla_{jk} = \frac{\sum_{n=j}^k G_n \delta T_n}{\sum_{n=j}^k G_n}, \quad (3)$$

in (2) encapsulates the change in transmission due to an integrated change in temperature between levels p_j and p_k , based on the precomputed weight vector \mathbf{G} for the reference state. The last two terms in (2) with coefficient matrices γ_{ij}^{01} and γ_{ij}^{02} represent the first- and second-order corrections due to the effects of integrated changes in CO_2 column density between levels j and k , where (Zhu, 1994)

$$\Pi_{jk} = \frac{\sum_{n=j}^k G_n \ln(r_n^{\text{CO}_2} / r_{0n}^{\text{CO}_2})}{\sum_{n=j}^k G_n (\ln 2 - \ln 0.5) / 2}. \quad (4)$$

Non-LTE correction of the Curtis matrix (2) follows the equivalent two-level approach of Zhu (1990) as summarized by the matrix equation (24) of Zhu et al. (1992). With a non-LTE-corrected \mathbf{C} thus computed, the cooling rate (1) follows by specifying the wide-band normalized source function column vector $\mathbf{\Theta} = \theta(\mathbf{T})$ at the band center frequency of $\nu_0 \sim 675 \text{ cm}^{-1}$:

$$\theta(T_k) = \frac{B(\nu_0, T_k)}{B(\nu_0, 200 \text{ K})} = \frac{127.38}{\exp\left(\frac{971 \text{ K}}{T_k}\right) - 1}, \quad (5)$$

where $B(\nu_0, T_k)$ is the Planck function. The source function is normalized in (5) by the Planck function value at 200 K so that \mathbf{C} , scaled by the same factor, yields approximate cooling-rate contributions in its matrix elements [this normalization factor cancels out of (1)]. The normalization temperature of 200 K in (1) is scaled down from the 250 K used for Earth by Zhu (1993) to reflect generally lower mean temperatures on Mars.

2.2. Computation and Validation of Mean Rates

We defined representative ranges of atmospheric variability by averaging vertical profiles of temperature, pressure, and CO_2 and O mixing ratios at a given latitude from the Mars Climate Database (MCD: Lewis et al., 1999). Solid curves in Figure 1 show mean and maximum/minimum profiles of various fields at 40°N under conditions of typical background dust loading and moderate solar EUV activity (Forget et al., 1999). The gray scale depicts the profile distribution density for the kinetic temperature T , CO_2 and O mixing ratios and O/ CO_2 mixing ratio.

The mean profiles in Figure 1 are used as our reference state for the cooling-rate computations and are interpolated to a height grid z_k ($k = 1 \dots L$) of resolution $\Delta z = 0.5$ km at $L = 401$ levels from the surface to 200 km. The reference Curtis matrix \mathbf{C}_0 and the various interpolation matrices in (2) were then calculated by the correlated- k distribution method (Lacis and Oinas, 1991; Zhu, 1994). The correlated- k coefficients and the temperature and pressure dependences were calculated by line-by-line integration using the 1986 HITRAN database (Rothman et al., 1987) for 20 different pressure levels (from 0 to 1100 hPa) and 7 reference temperatures from 150 K to 300 K (see Table 1 of Zhu et al., 1992). The entire CO_2 15- μm band ($525\text{--}825\text{ cm}^{-1}$) was divided into 12 equally spaced subbands and 30 Gaussian quadrature points were used in each subband to perform the integration (Zhu, 1994). Since the vibrational partition function of the CO_2 15- μm band is nearly constant, the coefficient was simply extrapolated to 100 K to cover the lower temperature range encountered in the atmosphere of Mars (see Figure 1b). The resulting reference matrices and vectors were saved as lookup tables for subsequent use in (2).

In addition to the standard modifications of physical constants, the following rate changes were made for Mars. For Earth, Zhu (1990) used deactivation rates of CO_2 ν_2 V-T emissions by collisions with air molecules (N_2 plus O_2) and O atoms from Dickinson (1984) and references

therein. For the predominantly CO₂ atmosphere of Mars, the former rate [eq. (73a) in Zhu (1990)] is replaced with a new rate based on collisional deactivation by other CO₂ molecules. For the $\nu_2 = 1 \rightarrow 0$ V-T transition we adopt the analytical fit (k_{5a}) in Table 3 of López-Valverde and López-Puertas (1994). The rate due to collisional deactivation by monatomic oxygen (O³P), k_{O-CO_2} , which has a large impact on high-altitude cooling rates, was originally 2×10^{-13} cm s⁻¹ in (73b) of Zhu (1990). It is reset here to 3×10^{-12} cm s⁻¹, based on recent modeling and laboratory work (e.g., Bougher et al., 1994; Khvorostovskaya et al., 2002; Castle et al., 2006), and is identical to the value for Mars used by López-Valverde and López-Puertas (1994) (their k_{7a}) and recommended by López-Valverde et al. (1998). Lacking measurements of the rates of $\nu_2 = 2 \rightarrow 1$ V-T transitions, López-Valverde and López-Puertas (1994) scaled their $\nu_2 = 1 \rightarrow 0$ rates by 2.5 and 2 for collisions with CO₂ and O³P, respectively, which we also adopt, the former rate replacing (72b) of Zhu (1990).

Figure 2a plots the mean kinetic temperature profile used by López-Valverde et al. (1998) to compute cooling rates using the more detailed Curtis-matrix Mars RT code of López-Valverde and López-Puertas (1994). Figure 2b plots the 15 μ m cooling rates from our interpolated Curtis matrix calculation using their temperature profile and mean profiles of O and CO₂ mixing ratio in Figures 1c and 1e, respectively. Despite differences in mixing ratio profiles and our simpler RT model, the cooling rates in Figure 2b are very similar in overall shape and magnitude to those of López-Valverde et al. (1998) (see their Figure 1b). Figure 3c shows variations in cooling rate for the mean 40°N profiles in Figure 1 as k_{O-CO_2} is halved and doubled. The cooling rates show a similar range of variability to that found in a similar sensitivity test of Mars cooling rates performed by López-Puertas and López-Valverde (1995) (see their Figure 6). Other tests (not shown) reveal similarly strong increases to those found by López-Puertas and López-Valverde (1995) when the profile of O³P mixing ratios is increased to values representative of solar maximum conditions.

Here and throughout this paper, we express our heating rates and damping rates in terms of Earth days (day⁻¹). Corresponding rates in terms of a Martian day (sol⁻¹) are obtained by multiplying these rates by 1.027491.

3. Vertical Scale-Dependent IR Radiative Damping Rates

Our approach to quantifying scale-dependent IR radiative damping of temperature perturbations closely follows that of Zhu and Strobel (1991) and Zhu (1993), who provide more details and justification.

If we add small temperature perturbations $\delta\mathbf{T}$ to a background temperature vector \mathbf{T}_b , linearization of (1) yields

$$\frac{d\delta\mathbf{T}}{dt} = \left[\mathbf{C} \frac{\partial \Theta}{\partial \mathbf{T}} \right]_b \delta\mathbf{T} + \delta\mathbf{C} \Theta_b, \quad (6)$$

where terms computed at the unperturbed temperature \mathbf{T}_b have the subscript “b.” Eq. (6) can be reexpressed, with the aid of matrix manipulations (Zhu and Strobel, 1991), as

$$\frac{d\delta\mathbf{T}}{dt} = \mathbf{D} \delta\mathbf{T}. \quad (7)$$

Calculations by Zhu and Strobel (1991) show that, for small $\delta\mathbf{T}$, contributions from the first term in (6) are an order of magnitude larger than from the second. Thus, to a good approximation

$$\mathbf{D} = \left[\mathbf{C} \frac{\partial \Theta}{\partial \mathbf{T}} \right]_b. \quad (8)$$

The linear system (7) and (8) describes nonlocal damping of temperature perturbations, and can be solved using either the eigenvalue or the Newtonian cooling approach (Goody and Yung, 1989). Both solutions were computed and compared by Zhu and Strobel (1991) and Zhu (1993). They found that, while each gave equivalent results in certain limits, the two solutions generally differed. They found that the most accurate solution overall was a Newtonian cooling rate that varied both with height and the vertical scale of the temperature perturbation, derived explicitly as (Sasamori and London, 1966; Zhu and Strobel, 1991)

$$\tau_r^{-1}(z, m) = - \int_{-\infty}^{\infty} K(z', z) \cos[m(z' - z)] dz', \quad (9)$$

where $K(z', z)$ is the kernel function (Spiegel, 1957), $m = 2\pi/\lambda_z$ is the vertical wavenumber of (assumed) sinusoidal eigenmodes, and $\tau_r(z, m)$ is the e-folding damping time scale of a sinusoidal temperature perturbation of wavenumber m due to infrared radiative cooling. Since (7) and (8) can be expressed equivalently as a discretized form of the integral relation (Zhu, 1993)

$$\frac{d\delta T(z)}{dt} = \int_{-\infty}^{+\infty} K(z', z) \delta T(z') dz', \quad (10)$$

then solutions to (9) follow by evaluating (7) and (8) at z_i using a perturbation temperature profile $\delta T(z') = \hat{T} \cos m(z' - z_i)$, whereupon $\tau_r^{-1}(z_i, m) = -\hat{T}^{-1} d\delta T(z_i)/dt$. The choice for \hat{T} is arbitrary since it has no impact on the final $\tau_r^{-1}(z_i, m)$ estimate due to the linear nature of the calculation.

We computed rates using the mean temperature and constituent profiles in Figure 1 as our background, for $\lambda_z = 2\pi/m$ values in the range 1-500 km. Figure 4 profiles the resulting $\tau_r^{-1}(z, m)$ estimates. We see strong vertical scale dependence in the rates at $z \lesssim 100$ km, with damping rates peaking at $\sim 30\text{--}40 \text{ days}^{-1}$ (i.e., e-folding times of <1 hour) at the shortest vertical scales at $z \sim 60\text{--}80$ km. The rates become largely scale-independent at $z \gtrsim 120$ km due to breakdown of LTE that yields an optically thin, transparent damping limit that is well approximated by a constant cooling-to-space term, due to negligible layer exchange.

Figure 5 profiles these radiative damping rates for different choices of $\lambda_z = 2\pi/m$. This plot resembles the presentation in Figure 4 of Zhu (1993) of corresponding CO_2 and O_3 damping rates for the Earth’s atmosphere. Comparisons between the two plots show that scale-dependent thermal damping rates due to $15 \mu\text{m}$ CO_2 cooling in the Martian atmosphere are, overall, about 20 times faster than on Earth. This finding is broadly consistent with an earlier Mars-Earth comparison of radiative damping rates by Imamura and Ogawa (1995). Figure 6 compares our scale-dependent rates with those of Imamura and Ogawa (1995), which were derived using the analytical approximations of Fels (1984). Our values are generally larger than theirs. A similar offset between the two rate calculations on Earth was noted by Zhu (1993), and ascribed to a more accurate treatment of non-LTE effects in the current approach relative to that of Fels (1982, 1984). Given other large differences between the two calculations (e.g., different mean temperatures, mixing ratios and rate coefficients; see below), there is reasonable overall agreement in Figure 6 between the rates from each calculation at all altitudes. Note in particular the transition from strong scale dependence at $z = 60\text{--}80$ km to an essentially scale-independent rate at $z \gtrsim 120$ km.

Our rates were computed using the mean background temperature $T_b(z)$ in Figure 1b, reproduced as the thick curve in Figure 7a, with the damping rate profile it yields at $\lambda_z = 5$ km also plotted in Figure 7b. Following Fels (1982), we can scale those reference rates to yield damping

rates at some other background temperature T as

$$\tau_r^{-1}(z, m; T) = \frac{\partial\theta/\partial T}{[\partial\theta/\partial T]_b} \tau_r^{-1}(z, m; T_b), \quad (11)$$

where, from (5),

$$\frac{\partial\theta}{\partial T} = 1.23686 \times 10^5 \text{ K} \left\{ \frac{\exp\left(\frac{971 \text{ K}}{T}\right)}{T^2 \left[\exp\left(\frac{971 \text{ K}}{T}\right) - 1\right]^2} \right\}. \quad (12)$$

Thin curves in Figure 7a plot temperature profiles offset from $T_b(z)$ by ± 5 K, ± 10 K and ± 20 K. The corresponding temperature-scaled rates $\tau_r^{-1}(z, m; T)$ at $\lambda_z = 5$ km from (11) and (12) are plotted with thin curves in Figure 7b. The rates show a strong dependence on background temperature through (12). The impact is particularly large at $z \sim 70$ – 120 km due to the low background temperatures at these altitudes which yields a larger relative change to (12), such that a uniform 10 K warmer atmosphere at all altitudes causes a doubling of the radiative damping rate at these altitudes.

Appendix A describes least-squares fits of our $\tau_r^{-1}(z, m; T_b)$ rates that can be used with (11) and (12) as a simple computationally-efficient parameterization of scale-dependent IR radiative damping rates.

4. Gravity Wave Damping

Following Marks and Eckermann (1995), we consider gravity waves governed by the anelastic dispersion relation

$$m^2 = \frac{(k^2 + l^2)(N^2 - \omega^{+2})}{\omega^{+2} - f^2} - \alpha^2. \quad (13)$$

Wave parameters are as follows: ω is ground-based frequency, $\omega^+ = \omega - Uk - Vl$ is intrinsic frequency, and (k, l, m) is the wavenumber vector. Background atmospheric variables are horizontal wind (U, V) , inertial frequency f , buoyancy frequency N , and $\alpha^2 = 1/4H_\rho^2$, where H_ρ is the density scale-height.

Gravity wave dissipation affects the larger-scale circulation through deposition of the wave momentum flux

$$\mathbf{F} = \rho_b (\overline{u'w'}, \overline{v'w'}) = (k, l) c_{gz} A. \quad (14)$$

Here (u', v', w') is the gravity wave-induced vector velocity anomaly, ρ_b is background density, c_{gz} is vertical group velocity, $A = E/\omega^+$ is wave action density, E is total (kinetic plus potential) wave energy, and overbars denote horizontal averages.

In the absence of dissipation, wave action density A is conserved through the continuity relation

$$\frac{\partial A}{\partial t} + \nabla \cdot (\mathbf{c}_g A) = 0, \quad (15)$$

where \mathbf{c}_g is the ground-based three-dimensional group velocity vector. In the absence of horizontal gradients and local time variations, the solution of (15) is a constant vertical flux of wave action, $c_{gz}A$, and thus constant momentum flux \mathbf{F} through (14), since (k, l) is also constant. Dissipation of gravity waves causes some fraction of the wave momentum flux (14) to be deposited locally, which in turn exerts a force $-\partial \mathbf{F} / \partial z$ on the background flow. Appendix B of Marks and Eckermann (1995) outlines how general mechanical and thermal dissipation terms in the linearized Navier Stokes equations yield net wave action dissipation terms on the right hand side of (15). Substituting standard expressions for viscous dissipation and thermal Newtonian damping, the net dissipation of wave action density can be expressed in the Newtonian damping form (Marks and Eckermann, 1995)

$$\frac{\partial A}{\partial t} + \nabla \cdot (\mathbf{c}_g A) = -\frac{2A}{\tau_w}, \quad (16)$$

where the damping rate of gravity-wave amplitudes

$$\tau_w^{-1} = \frac{\tau_r^{-1} \left(\frac{1-f^2/\omega^+}{1-\omega^+/N^2} \right) + \tau_v^{-1} \left(1 + \frac{f^2}{\omega^+} + \frac{1-f^2/\omega^+}{N^2/\omega^+-1} + Pr^{-1} \frac{1-f^2/\omega^+}{1-\omega^+/N^2} \right)}{\left[1 + \frac{f^2}{\omega^+} + \frac{N^2+\omega^+}{N^2-\omega^+} \left(1 - \frac{f^2}{\omega^+} \right) \right]}, \quad (17)$$

$$= \tau_{wr}^{-1} + \tau_{wv}^{-1} = w_r \tau_r^{-1} + w_v \tau_v^{-1}. \quad (18)$$

In (17), τ_r^{-1} is the scale-dependent IR radiative damping rate (11), $\tau_v^{-1} = \eta(k^2 + l^2 + m^2 + \alpha^2)$ is the viscous damping rate, η is the kinematic viscosity and Pr is the Prandtl number. In the equivalent form (18), τ_{wr}^{-1} and τ_{wv}^{-1} are the damping rates of gravity-wave amplitudes due to IR radiative cooling and viscous dissipation, respectively. These in turn depend on the gravity-wave weighting coefficients for radiative damping, w_r , and viscous damping, w_v . Figure 8 shows how

they vary as intrinsic frequency ω^+ is varied from the low-frequency limit ($f^2/\omega^{+2} \sim 1$) through to a nominal high-frequency limit of $\omega^{+2}/N^2 \rightarrow 1$ (note that gravity waves governed by (13) have a high-frequency limit ω_c^+ that is typically less than N : see Marks and Eckermann, 1995). The variations in Figure 8 are due to the polarization characteristics of gravity waves. For example, the vanishing of w_v (and hence τ_{wv}^{-1}) as $\omega^{+2} \rightarrow f^2$ is due to an enhancement in wave kinetic energy at the expense of wave potential energy, which reduces wave-induced temperature perturbations and thus the net impact of thermal damping on wave action. Note too the strong sensitivity of the viscous damping of gravity waves to the Prandtl number.

Below the turbopause, viscous damping has both molecular and turbulent contributions. Since the Prandtl numbers of each vary, to treat both forms of viscous damping it proves necessary to further subdivide the viscous gravity-wave damping τ_{wv}^{-1} in (18) into the sum of separate molecular and turbulent contributions, given in each case by the second term on the right-hand side of (17), but in each instance substituting the relevant molecular or turbulent viscosity (η_m or η_t , respectively) and Prandtl number (Pr_m or Pr_t , respectively): i.e.,

$$\tau_{wv}^{-1} = w_{vm}\tau_{vm}^{-1} + w_{vt}\tau_{vt}^{-1}. \quad (19)$$

Since turbulent viscosities η_t on Mars are poorly constrained (see, e.g., Bittner and Fricke, 1987; Chassefiere et al., 1994; Izakov, 2007), we defer their treatment and discussion until later in the paper, and consider for now just the molecular viscosity contribution. We specify kinematic molecular viscosities as

$$\eta_m = \frac{9.18 \times 10^{-8} T_b^{0.91}}{\rho_b}. \quad (20)$$

The numerator in (20) is a least-squares fit to molecular viscosities (in units of $\text{kg m}^{-1} \text{s}^{-1}$) over the 50-500 K range from laboratory measurements for a Mars-like mixture of gases, taken from Table 1 of Catalfamo et al. (2009). In the $T_b=100\text{--}400$ K range, data in Tables 1-2 of Catalfamo et al. (2009) yield $Pr_m \sim 0.7\text{--}0.95$, while a representative Martian $C_p = 805 \text{ J kg}^{-1} \text{ K}^{-1}$ yields $Pr_m \sim 0.89$ when applied to the same data. We adopt a median value of $Pr_m = 0.8$, slightly larger than $Pr_m = 0.71$ for the Earth's atmosphere, consistent with theory and laboratory measurements that a mostly triatomic molecular atmosphere of CO_2 should have a slightly higher Prandtl number than the mostly diatomic atmosphere of Earth.

The inverse density dependence in (20) yields an exponential increase in η_m with height, so that local molecular viscous damping will eventually exceed the local IR radiative damping of waves at some altitude z_v . Imamura and Ogawa (1995) estimated z_v to be ~ 120 km on Mars. We used the gravity-wave equations above to calculate z_v based on mean temperature and density profiles in Figure 1 that specify both our τ_r^{-1} rates from Figure 4 and our η_m values from (20). The profiles of N and H_ρ based on this mean temperature profile are plotted in Figure 9. To keep these initial calculations simple, here we adopt constant values, based on approximate profile means in Figure 9, of $N = 0.01 \text{ rad s}^{-1}$ and $H_\rho = 9.5 \text{ km}$, so that m in (13) remains constant (later calculations will remove this assumption). We set $f = 10^{-4} \text{ s}^{-1}$, corresponding to a latitude of 45°N . Figure 10 plots the altitude at which τ_{wv}^{-1} first exceeds τ_{wr}^{-1} as a function of vertical wavenumber m and total horizontal wavenumber $K_{tot} = (k^2 + l^2)^{1/2}$. We find a strong variation of z_v with m , varying from ~ 80 km at $\lambda_z \sim 1 \text{ km}$ to ~ 140 km at $\lambda_z \sim 100 \text{ km}$.

To study in greater depth the impact of radiative damping relative to other gravity-wave damping mechanisms on Mars, we developed a simple one-dimensional anelastic gravity-wave model based on the dispersion relation (13) and its associated linear gravity-wave equations, as described in Appendix B. The model simulates gravity-wave propagation and amplitude evolution through a vertical atmospheric column extending from the surface to 200 km using the same height grid z_k as for the radiation calculations. Peak vertical displacement amplitudes $\hat{\zeta}(z)$ and momentum fluxes $F(z) = |\mathbf{F}(z)|$ are computed subject to radiative and molecular viscous damping, and amplitude saturation due to wave breaking. The model is a slightly more complicated version of the one-dimensional formulations used in gravity-wave drag parameterizations (Joshi et al., 1996; Collins et al., 1997; Forget et al., 1999). Although background horizontal winds $U(z)$ and $V(z)$ are included in the model, for simplicity we set $U = V = 0$ so that large wavenumber refraction effects are eliminated, allowing us to more effectively study dissipation as a function of vertical wavenumber at a range of altitudes. Since IR radiative damping rates are acutely temperature sensitive (see Figure 7), the simulated gravity waves propagate through the realistic background temperature $T_b(z)$ shown in Figures 1b and 7a. For consistency, our model calculations include the resulting height variations in N and H_ρ shown in Figure 9, which cause m values to vary slightly with height through the dispersion relation (13).

For each wave, we must choose a launch (source) altitude, z_s , and an initial peak vertical displacement amplitude, $\hat{\zeta}(z_s)$. We choose $z_s = 0$ on the assumption that major gravity-wave sources are located in the lower atmosphere, such as waves forced by flow over mesoscale terrain (Joshi et al., 1996). There are few observations to reliably guide our choice for $\hat{\zeta}(z_s)$. On Earth, mean gravity-wave amplitudes are controlled by vertical wavenumber spectra with highly reproducible shapes that peak in variance at a characteristic vertical wavenumber, m_* , which is typically in the range $2\pi(1-3 \text{ km})^{-1}$ in the lower atmosphere (Allen and Vincent, 1995). While there have been no measurements of vertical wavenumber spectra on Mars to date, the observed horizontal wavenumber spectra of Imamura et al. (2007) bear a strong resemblance to those measured on Earth in the mesoscale range, which in turn suggests theoretically that vertical wavenumber spectra should also have somewhat similar shapes (see, e.g., Bacmeister et al., 1996). The total vertical displacement variance, obtained by integrating canonical forms for gravity-wave vertical wavenumber spectra observed on Earth, is $\sim 0.1m_*^2$ (Fritts and VanZandt, 1993), which, on choosing a representative $m_* = 2\pi(2 \text{ km})^{-1}$ for the lower atmosphere, yields an r.m.s. wave-induced vertical displacement of 100 m. Given conflicting evidence as to whether gravity-wave amplitudes are weaker or stronger on Mars relative to Earth (see section 5), we adopt the default assumption of similar wave amplitudes and thus set $\zeta(z_s) = 100 \text{ m}$ for our simulations.

Figure 11 plots $\hat{\zeta}(z)$ (left panel) and $F(z)$ (right panel) for a gravity wave of $\lambda_h = 2\pi/K_{tot} = 100 \text{ km}$ and ground-based phase speed $c \sim 3.6 \text{ m s}^{-1}$ which yields a source-level vertical wavelength $\lambda_z = 2\pi/|m(z_s)| = 2.5 \text{ km}$. The thick gray curves in Figure 11 show gravity-wave solutions in which no dissipation has been applied, whereupon $F(z)$ remains constant with height and $\hat{\zeta}(z)$ grows with height roughly as $\rho_b^{-1/2} \propto \exp \int dz/2H_\rho$. The thick gold curves are solutions in which only wave breaking/saturation has been applied, which is the standard parameterization approach (Joshi et al., 1996; Collins et al., 1997; Forget et al., 1999). The black dashed (blue dotted) curve is the solution in which only IR radiative (molecular viscous) damping has been applied, with the solid aqua curve showing solutions with both IR radiative and molecular viscous damping applied. The red curve shows the solution in which all three damping processes (IR radiative damping, molecular viscous damping, and saturation due to wave breaking) were applied. The results in Figure 11 show that the amplitude evolution of this wave is dominated by IR radiative

damping. The IR damping of this wave is so severe that $\zeta(z)$ decreases with altitude in Figure 11a and never attains a threshold amplitude for wave breaking.

Figure 12 shows corresponding solutions for a wave of ground-based phase speed $c \sim 6.6 \text{ m s}^{-1}$, which yields a source-level vertical wavelength $\lambda_z = 2\pi/|m(z_s)| = 5 \text{ km}$. While wave amplitudes grow slowly with altitude in this example up to $\sim 40 \text{ km}$ altitude, they are strongly dissipated above 40 km and again do not attain breaking amplitudes at any altitude. Dissipation of wave amplitude and momentum flux is again dominated by the IR radiative damping term.

Figure 13 plots solutions for a wave of $c \sim 12.9 \text{ m s}^{-1}$, which yields a source-level vertical wavelength $\lambda_z = 2\pi/|m(z_s)| = 10 \text{ km}$. This wave grows in amplitude with height and attains a breaking amplitude at $\sim 60 \text{ km}$, whereupon it continues breaking as a saturated wave up to $\sim 100 \text{ km}$ before being rapidly dissipated by molecular viscosity thereafter. Clearly, all three damping mechanisms (IR radiative cooling, molecular viscosity, and wave breaking) play a role in progressively depositing this wave's momentum flux throughout the atmospheric column. To assess the relative contributions, the red curve in Figure 13c plots the cumulative percentage of the wave's original momentum flux that has been deposited into the background flow for the simulation in which all three damping processes were activated, showing that essentially 100% of the wave's momentum flux has been dissipated by the time the wave has propagated to $z \sim 100 \text{ km}$. The remaining curves in Figure 13c show the contributions to this total from saturation (gold curve), IR radiative damping (black dashed curve), molecular viscosity (blue dotted curve) and radiative plus molecular damping (aqua curve). These results show that $\sim 90\%$ of this wave's momentum flux was dissipated by IR radiative damping, $\sim 10\%$ by wave breaking (saturation), and $<1\%$ by molecular viscosity.

Only on progressing to Figure 14, which plots solutions for a wave of $c \sim 19.0 \text{ m s}^{-1}$ ($\lambda_z = 2\pi/|m(z_s)| = 15 \text{ km}$), do we see wave breaking/saturation become competitive with IR radiative damping in dissipating wave momentum flux. In this example, Figure 14c reveals that wave breaking accounts for slightly more than 50% of the overall flux deposition through the column, and IR radiative damping accounts for slightly less than 50%. Again, molecular viscous damping is essentially negligible, acting only to damp out the tiny momentum flux residual that remains at high altitudes.

To provide a broader integrated picture, we conducted a series of simulations like those in Figures 11–14 for a range of waves with different source-level vertical wavenumbers $m(z_s)$, with all physical damping processes activated in each case. Figure 15a plots the cumulative percentage of dissipated momentum flux as a function of z and $|m|$ for waves of $K_{tot} = 2\pi(100 \text{ km})^{-1}$. The contributions to the percentage totals in Figure 15a from wave breaking/saturation, molecular viscous damping, and IR radiative damping, are plotted in Figures 15b, 15c and 15d, respectively. In all cases, molecular viscous damping accounts for much less than 1% of the total flux deposition. At low altitudes, IR radiative damping is the dominant momentum-flux dissipation mechanism for all the waves, and it remains dominant at higher altitudes for those gravity waves of $\lambda_z(z_s) \lesssim 15 \text{ km}$. At higher altitudes, saturation eventually becomes the dominant flux deposition process for gravity waves of $\lambda_z(z_s) \gtrsim 15 \text{ km}$, accounting for $> 90\%$ of the flux deposition for waves with $\lambda_z(z_s) > 40 \text{ km}$.

These findings are highlighted in a slightly different way in Figures 15e and 15f, which plot the ratio of saturation and IR radiative damping percentages, respectively, to the overall local flux deposition percentage in Figure 15a. Contours exist only in the top-left regions of these panels, with the remaining “blank” regions corresponding to a broad area of m – z space where the saturation contribution to the momentum-flux dissipation is $< 1\%$, and the IR radiative damping contribution is $> 99\%$. This highlights the major role played by IR radiative damping in controlling the momentum flux deposition of these waves.

Figure 16 plots “top-of-the-atmosphere” momentum-flux deposition percentages at $z = 200 \text{ km}$ due to each gravity-wave dissipation process, resulting from 3600 individual gravity-wave simulations spanning the indicated range of horizontal and vertical wavenumber pairings. Figure 16b again reveals a large area of this two-dimensional wavenumber space where IR radiative damping is the dominant flux deposition process. Molecular viscous damping is again very small for every wavenumber pairing considered. Wave breaking is significant only at longer vertical wavelengths and shorter horizontal wavelengths, which is consistent with the faster vertical group velocities at these wave scales that yield less time-integrated IR radiative damping along the ray path, in addition to the smaller radiative damping rates that occur at long vertical wavelengths in Figure 4.

5. Discussion and Conclusions

While faster radiative relaxation rates on Mars relative to Earth were inferred more than 40 years ago by Goody and Belton (1967), the damping of small vertical-scale temperature structure on Mars by $15\ \mu\text{m}$ CO_2 cooling has remained largely unquantified. In particular, it has remained unclear whether longwave radiative cooling yields significant thermal damping of gravity-wave momentum fluxes. The parameterizations of gravity-wave drag currently included within Mars GCMs do not include it, and thus tacitly assume that it is a secondary, negligible effect.

Using a Curtis matrix model of $15\ \mu\text{m}$ radiative cooling specifically adapted for Mars, we computed scale-dependent IR radiative damping rates $\tau_r^{-1}(z, m)$ from $z = 0$ –200 km over a vertical wavelength band from 1–500 km, for a representative mean Martian atmosphere at 40°N . We then used those rates to study the impact of IR radiative damping on the dissipation of gravity wave momentum fluxes, and compared it to those of other gravity-wave dissipation processes, such as wave breaking (saturation) and molecular viscous dissipation. Using a linear gravity wave model governed by simple anelastic wave physics, our results suggest that IR radiative damping is the dominant process by which gravity wave momentum flux is dissipated on Mars at altitudes below ~ 50 km, and is also the dominant flux-dissipating process at all altitudes for those waves whose vertical wavelengths are $\lesssim 10$ –15 km (see Figures 15 and 16).

The precise demarcations with altitude and wavenumber summarized in Figures 15 and 16 depend on a number of specific assumptions adopted in our modeling. For example, source-level gravity-wave amplitudes $\hat{\zeta}(z_s)$ could be much larger than our current choice of 100 m, which would cause waves to break at lower altitudes and thus increase the role of wave breaking. Different background thermal conditions will also reduce (or increase) radiative damping rates. We ran a series of simulations in which these and other choices were varied. While the locations of the contours in Figures 15 and 16 can vary in response, the overall morphology does not change markedly, and hence the major conclusions that we drew from the large-scale features evident in these results also do not change in any substantial way: Specifically,

- IR radiative damping is the dominant momentum-flux dissipation mechanism for all gravity waves in the lower atmosphere and lower regions of the middle atmosphere;

- for gravity waves whose source-level vertical wavelengths are $\lesssim 10\text{--}15$ km, IR radiative damping is the dominant momentum-flux dissipation mechanism at all altitudes;
- molecular viscosity has negligible impact on the total flux deposition of gravity waves; and,
- wave breaking is the dominant flux dissipation mechanism for “fast” gravity waves of short horizontal wavelength and/or long vertical wavelengths, which escape major IR damping at lower altitudes and deposit the majority of their momentum flux through wavebreaking and saturation at higher altitudes.

In short, our results strongly suggest that scale-dependent IR radiative damping is a first-order, and frequently dominant, mechanism by which gravity-wave amplitudes are dissipated on Mars, and hence exerts an important influence on gravity-wave momentum flux deposition and the wave-driven circulation of Mars.

Parameterizations of subgrid-scale orographic gravity-wave drag currently embedded within Mars GCMs are adapted from similar parameterizations in Earth GCMs, which only parameterize flux deposition due to wave breaking and saturation (Joshi et al., 1996; Collins et al., 1997; Forget et al., 1999). As Read and Lewis (2004) discuss in their review of gravity-wave drag effects on the Martian climate (chapter 4.4.4), when these parameterizations were initially adapted for and embedded within Mars GCMs, the parameterized source-level wave momentum fluxes had to be reduced by 1-2 orders of magnitude to produce a realistic climate (e.g., Collins et al., 1997). Taken at face value, this would imply much weaker orographic forcing of gravity-wave momentum flux on Mars relative to Earth. Yet surface flow patterns, and particularly orographic relief, would (if anything) seem to suggest the opposite, and the limited direct measurements of high-altitude gravity waves on Mars to date seem to support this countervailing viewpoint (e.g., Fritts et al., 2006).

The calculations presented in this paper lead us to propose an alternative explanation of this result. Our results reveal appreciable IR radiative damping of the momentum flux of all gravity wave at altitudes $z \sim 0\text{--}50$ km. This radiative damping prevents short vertical wavelength gravity waves from attaining breaking amplitudes (e.g., Figures 11 and 12), and causes waves of intermediate and longer vertical wavelength to break at higher altitudes (e.g., Figure 13), where the

wave possesses less remaining momentum flux to deposit via wave breaking and thus produces a weaker local mean-flow acceleration. For parameterizations that lack a model of scale-dependent IR radiative damping, the only way to tune the parameterization to compensate for this missing physics is to artificially reduce wave amplitudes at the source, so that waves break higher and deposit less momentum flux via breaking.

More work is needed to ascertain the exact ways in which IR radiative damping and wave breaking combine to control the deposition of gravity-wave momentum flux throughout the Martian atmosphere and in turn drive a large-scale wave-driven circulation. As on Earth, a major controlling factor will be the form of the background Martian winds $U(z)$ and $V(z)$. In this initial work, we deliberately omitted the complicating effects of mean wind shear and vertical wavenumber refraction by setting $U = V = 0$, to focus more easily on the relative impacts of IR damping relative to other processes as a function of height and wave scale, using waves of roughly constant frequency and wavenumber. Traditionally, westerly zonal winds $U(z)$ and westerly shear, for example, are viewed as progressively removing gravity waves with westerly phase speeds c at critical levels as $\omega^{+2} \rightarrow f^2$. Our results strongly suggest that such waves will be heavily dissipated by IR radiative damping as their vertical wavelengths contract, and will be “radiatively quenched” well before reaching either wave-breaking amplitudes or being absorbed at a critical level. Those easterly phase-speed waves propagating against the westerly flow will refract to longer vertical wavelengths, attain fast vertical group speeds, and thus may refract into regions of wavenumber space where upper-level wave breaking may be dominant (see Figures 15e and 16a). The situation becomes complicated since wave breaking conditions also vary strongly in response to background winds and shear. Generalization to three dimensions with variable wind and wave vector azimuths further complicates the picture, as does the nature and distribution of wave sources, making estimates of relative impacts complicated and case-specific. While these arguments indicate that more detailed model studies are needed to fully quantify such effects, we believe that the results presented here already present a sufficiently strong and compelling case to consider IR radiative damping an indispensable component of any parameterization that seeks to model gravity-wave momentum flux deposition accurately, as is required in GCMs. As described in Appendices A and B, the first order effects of IR radiative damping could be incorporated into existing gravity-

wave models and parameterizations with little increase in overall computational complexity and overhead.

To date, strong similarities have been noted between gravity-wave dynamics on Earth and Mars (e.g., Pirraglia, 1976; Pickersgill and Hunt, 1979; Tobie et al., 2003; Imamura et al., 2007; Parrish et al., 2009). This is reflected in the GCM parameterizations of gravity-wave drag for both planetary atmospheres, which at present possess almost identical governing physics (e.g., Forget et al., 1999; Medvedev and Hartogh, 2007). Our results point to a major physical difference in gravity-wave dissipation on each planet. On Earth, IR radiative damping is much weaker and wave breaking is the dominant flux dissipation process (Marks and Eckermann, 1995), and so gravity-wave dissipation is characterized by instability, overturning, turbulence generation and turbulent mixing. By contrast, we find IR radiative damping of gravity waves to be a major (often dominant) gravity-wave dissipation process on Mars. The IR radiative damping of gravity-wave momentum and energy fluxes, while producing mean-flow accelerations and frictional heating, respectively, does not (in and of itself) generate wave-field instabilities and turbulence. This in turn impacts the potential role of a fourth wave-damping mechanism, raised earlier in this paper [see eq. (19)] but thereafter ignored in our modeling: dissipation due to background turbulent diffusion. In the Earth's middle atmosphere, most turbulence is generated by gravity-wave breaking. If, as our results suggest, IR radiative damping reduces the amount of gravity-wave flux on Mars available for wave breaking (and hence turbulence generation), it would (all other things being equal) reduce gravity-wave-induced turbulence levels on Mars relative to Earth, as well as the overall impact of wave damping due to background turbulent diffusion and the turbulent vertical diffusion and mixing of trace constituents in the Martian middle atmosphere.

6. Acknowledgements

This research was partially supported by the Office of Naval Research, through the Naval Research Laboratory 6.1 work unit "Subgridscale Dynamics of Middle and Upper Atmospheres."

References

- Allen, S.J., Vincent, R.A., 1995. Gravity wave activity in the lower atmosphere: Seasonal and latitudinal variations. *J. Geophys. Res.* 100, 1327–1350.
- Bacmeister, J.T., Eckermann, S.D., Newman, P.A., Lait, L., Chan, K.R., Loewenstein, M., Proffitt, M.H., Gary, B.L., 1996. Stratospheric horizontal wavenumber spectra of winds, potential temperature, and atmospheric tracers observed by high-altitude aircraft. *J. Geophys. Res.* 101, 9441–9470.
- Bittner, H., Fricke, K.H., 1987. Dayside temperatures of the Martian upper atmosphere. *J. Geophys. Res.* 92, 12045–12055.
- Bougher, S.W., Hunten, D.M., Roble, R.G., 1994. CO₂ cooling in terrestrial planet thermospheres. *J. Geophys. Res.* 99, 14609–14622.
- Bresser, G., Manning, A.J.L., Pawson, S., Rodgers, C.D., 1995. A new parameterization of scale-dependent radiative rates in the stratosphere. *J. Atmos. Sci.* 52, 4429–4447.
- Castle, K.J., Kleissas, K.M., Rhinehart, J.M., Hwang, E.S., Dodd, J.A., 2006. Vibrational relaxation of CO₂ by atomic oxygen. *J. Geophys. Res.* 111, A09303, doi:10.1029/2006JA011736.
- Catalfamo, C., Bruno, D., Colonna, G., Laricchiuta, A., Capitelli, M., 2009. High temperature Mars atmosphere. Part ii: transport properties. *Eur. Phys. J. D* 54, 613–621.
- Chassefiere, E., Rosenqvist, J., Théodore, B., 1994. Ozone as a tracer of turbulence induced by breaking gravity waves on Mars. *Planet. Space Sci.* 42, 825–830.
- Collins, M., Lewis, S.R., Read, P.L., 1997. Gravity wave drag in a global circulation model of the Mars atmosphere: Parameterization and validation. *Adv. Space. Res.* 19, 1245–1254.
- Creasey, J.E., Forbes, J.M., Keating, G.M., 2006. Density variability at scales typical of gravity waves observed in Mars' thermosphere by the MGS accelerometer. *Geophys. Res. Lett.* 33, L22814, doi:10.1029/2006GL027583.
- Dickinson, R.E., 1984. Infrared radiative cooling in the mesosphere and lower thermosphere. *J. Atmos. Terr. Phys.* 46, 995–1008.
- Eckermann, S.D., Marks, C.J., 1997. GROGRAT: A new model of the global propagation and dissipation of atmospheric gravity waves. *Adv. Space Res.* 20(6), 1253–1256.
- Fels, S.B., 1982. A parameterization of scale-dependent radiative damping rates in the middle atmosphere. *J. Atmos. Sci.* 39, 1141–1152.
- Fels, S.B., 1984. The radiative damping of short vertical scale waves in the mesosphere. *J. Atmos. Sci.* 41, 1755–1764.
- Fels, S.B., Schwarzkopf, M.D., 1981. An efficient, accurate algorithm for calculating CO₂ 15 μ m band cooling rates. *J. Geophys. Res.* 86, 1205–1232.
- Fomichev, V.I., 2009. The radiative energy budget of the middle atmosphere and its parameterization in general circulation models. *J. Atmos. Sol.-Terr. Phys.* 71, 1577–1585.
- Forget, F., Hourdin, F., Fournier, R., Hourdin, C., Talagrand, O., Collins, M., Lewis, S.R., Read, P.L., Huot, J.P., 1999.

- Improved general circulation models of the Martian atmosphere from the surface to above 80km. *J. Geophys. Res.* 104, 24155–24176.
- Fritts, D.C., Rastogi, P.K., 1985. Convective and dynamical instabilities due to gravity wave motions in the lower and middle atmosphere. *Radio Sci.* 20, 1247–1277.
- Fritts, D.C., VanZandt, T.E., 1993. Spectral estimates of wave energy and momentum fluxes. Part i: Energy dissipation, acceleration, and constraints. *J. Atmos. Sci.* 50, 3685–3694.
- Fritts, D.C., Wang, L., Tolson, R.H., 2006. Mean and gravity wave structures and variability in the Mars upper atmosphere inferred from Mars Global Surveyor and Mars Odyssey aerobraking densities. *J. Geophys. Res.* 111, A12304, doi:10.1029/2006JA011897.
- González-Galindo, F., Forget, F., LópezValverde, M.A., i Coll, M.A., Millour, E., 2009. A ground-to-exosphere Martian general circulation model: 1. Seasonal, diurnal, and solar cycle variation of thermospheric temperatures. *J. Geophys. Res.* 114, E04001, doi:10.1029/2008JE003246.
- Goody, R., Belton, M.J.S., 1967. Radiative relaxation times for Mars: a discussion of Martian atmospheric dynamics. *Planet. Space Sci.* 15, 247–256.
- Goody, R.M., Yung, Y.L., 1989. *Atmospheric Radiation: Theoretical Basis*. Oxford University Press. second edition.
- Imamura, T., Kawasaki, Y., Fukuhara, T., 2007. Mesoscale spectra of Mars's atmosphere derived from MGS TES infrared radiances. *J. Atmos. Sci.* 64, 1717–1726.
- Imamura, T., Ogawa, T., 1995. Radiative damping of gravity waves in the terrestrial planetary atmospheres. *Geophys. Res. Lett.* 22, 267–270.
- Izakov, M.N., 2007. Turbulence in the free atmospheres of Earth, Mars, and Venus: A review. *Sol. Syst. Res.* 41, 355–384.
- Joshi, M.M., Lawrence, B.N., Lewis, S.R., 1996. The effect of spatial variations in unresolved topography on gravity wave drag in the Martian atmosphere. *Geophys. Res. Lett.* 23, 2927–2930.
- Khvorostovskaya, L.E., Potekhin, I.Y., Shved, G.M., Ogibalov, V.P., Uzyukova, T.V., 2002. Measurement of the rate constant for quenching CO₂ [01¹0] by atomic oxygen at low temperatures: Reassessment of the rate of cooling by the CO–2 15μm emission in the lower thermosphere. *Atmos. Ocean. Phys.* 38, 613–624.
- Kleinböhl, A., Schofield, J.T., Kass, D.M., Abdou, W.A., Backus, C.R., Sen, B., Shirley, J.H., Lawson, W.G., Richardson, M.I., Taylor, F.W., Teanby, N.A., McCleese, D.J., 2009. Mars Climate Sounder limb profile retrieval of atmospheric temperature, pressure, and dust and water ice opacity. *J. Geophys. Res.* 114, E10006, doi:10.1029/2009JE003358.
- Kutepov, A.A., Gusev, O.A., Ogibalov, V.P., 1998. Solution of the non-LTE problem for molecular gas in planetary atmospheres: Superiority of accelerated lambda iteration. *J. Quant. Spectrosc. Radiat. Transfer* 60, 199–220.
- Lacis, A.A., Oinas, V., 1991. A description of the correlated *k* distribution method for modeling nongray gaseous absorption, thermal emission, and multiple scattering in vertically inhomogeneous atmospheres. *J. Geophys. Res.*

96, 9027–9063.

- Lewis, S., Collins, M., Read, P., Forget, F., Hourdin, F., Fournier, R., Hourdin, C., Talagrand, O., Huot, J., 1999. A climate database for Mars. *J. Geophys. Res.* 104, 24177–24194.
- López-Puertas, M.L., López-Valverde, M.A., 1995. Radiative energy balance of CO₂ non-LTE infrared emissions in the Martian atmosphere. *Icarus* 114, 113–129.
- López-Valverde, M.A., Edwards, D.P., López-Puertas, M., Roldan, C., 1998. Non-local thermodynamic equilibrium in general circulation models of the Martian atmosphere 1. Effects of the local thermodynamic equilibrium approximation on thermal cooling and solar heating. *J. Geophys. Res.* 103, 16,799–16,811.
- López-Valverde, M.A., López-Puertas, M., 1994. A non-local thermodynamic equilibrium radiative transfer model for infrared emissions in the atmosphere of Mars, 1. Theoretical basis and nighttime populations of vibrational levels. *J. Geophys. Res.* 99, 13,093–13,115.
- Marks, C.J., Eckermann, S.D., 1995. A three-dimensional nonhydrostatic ray-tracing model for gravity waves: Formulation and preliminary results for the middle atmosphere. *J. Atmos. Sci.* 52, 1959–1984.
- Medvedev, A.S., Hartogh, P., 2007. Winter polar warmings and the meridional transport on Mars simulated with a general circulation model. *Icarus* 186, 97–110.
- Parrish, H.F., Schubert, G., Hickey, M.P., Walterscheid, R.L., 2009. Propagation of tropospheric gravity waves into the upper atmosphere of Mars. *Icarus* 203, 28–37.
- Pickersgill, A.O., Hunt, G.E., 1979. The formation of Martian lee waves generated by a crater. *J. Geophys. Res.* 84, 8317–8331.
- Pirraglia, J.A., 1976. Martian atmospheric lee waves. *Icarus* 27, 517–530.
- Read, P.L., Lewis, S.R., 2004. *The Martian Climate Revisited: Atmosphere and Environment of a Desert Planet*. Springer-Verlag.
- Richardson, M.I., Toigo, A.D., Newman, C.E., 2007. PlanetWRF: A general purpose, local to global numerical model for planetary atmospheric and climate dynamics. *J. Geophys. Res.* 112, E09001, doi:10.1029/2006JE002825.
- Rothman, L.S., Gamache, R.R., Goldman, A., Brown, L.R., Toth, R.A., Pickett, H.M., Poynter, R.L., Flaud, J.M., Camy-Peyret, C., Barbe, A., Husson, N., Rinsland, C.P., Smith, M.A.H., 1987. The HITRAN database: 1986 edition. *Appl. Opt.* 26, 4058–4097.
- Sasamori, T., London, J., 1966. The decay of small temperature perturbations by thermal radiation in the atmosphere. *J. Atmos. Sci.* 23, 543–554.
- Shved, G.M., Utyakovsky, D.P., 1983. Radiative damping of temperature perturbations in the Earth's upper atmosphere with allowance for departure from local thermodynamic equilibrium. *Izv. Akad. Nauk S.S.S.R. Atmos. Oceanic Phys.* 19, 476–482.
- Spiegel, E.A., 1957. The smoothing of temperature fluctuations by radiative transfer. *Astrophys. J.* 126, 202–207.
- Tobie, G., Forget, F., Lott, F., 2003. Numerical simulation of the winter polar wave clouds observed by Mars Global

- Surveyor Mars Orbiter Laser Altimeter. *Icarus* 164, 33–49.
- Zhu, X., 1990. Carbon dioxide 15- μm band cooling rates in the upper middle atmosphere calculated by Curtis matrix interpolation. *J. Atmos. Sci.* 47, 755–774.
- Zhu, X., 1993. Radiative damping revisited: Parameterization of damping rate in the middle atmosphere. *J. Atmos. Sci.* 50, 3008–3021.
- Zhu, X., 1994. An accurate and efficient radiation algorithm for middle atmosphere models. *J. Atmos. Sci.* 51, 3593–3614.
- Zhu, X., Strobel, D.F., 1990. On the role of vibration-vibration transitions in the radiative cooling of the CO₂ 15 μm band around the mesopause. *J. Geophys. Res.* 95, 3571–3577.
- Zhu, X., Strobel, D.F., 1991. Radiative damping in the upper mesosphere. *J. Atmos. Sci.* 48, 184–199.
- Zhu, X., Summers, M.E., Strobel, D.F., 1992. Calculation of CO₂ 15- μm band atmospheric cooling rates by Curtis matrix interpolation of correlated-k coefficients. *J. Geophys. Res.* 97, 12787–12797.

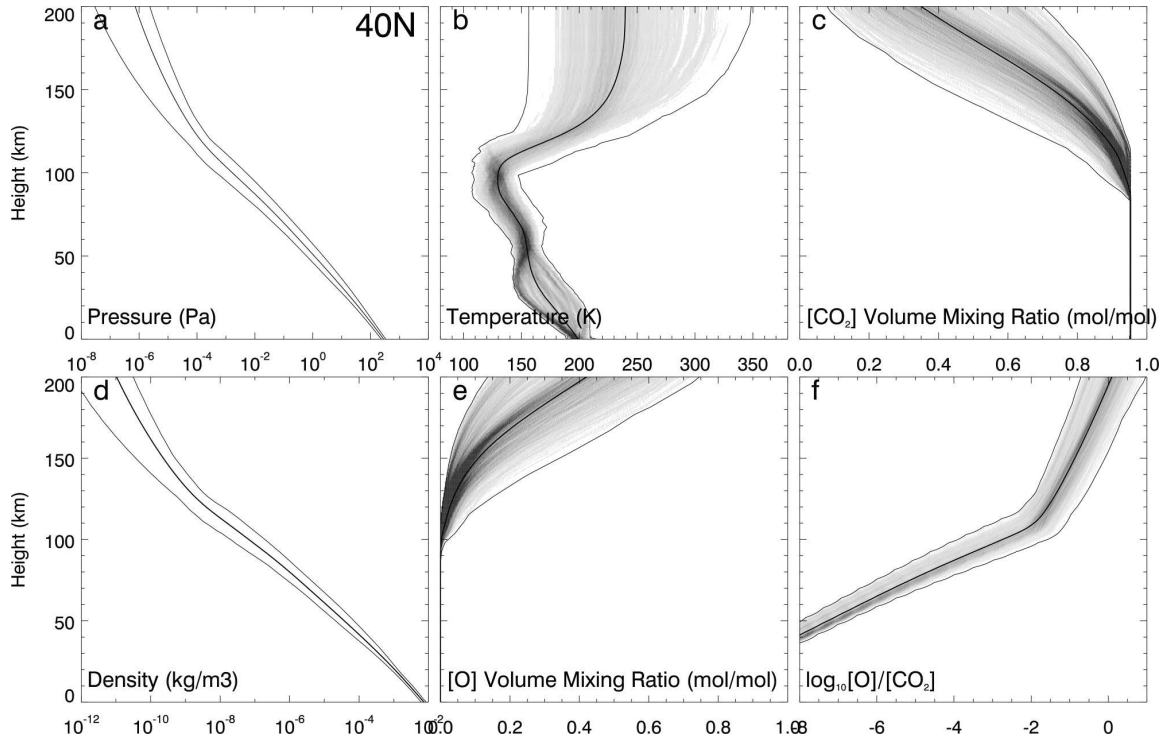


Figure 1: Profiles of (a) pressure, (b) temperature, (c) CO_2 volume mixing ratio, (d) density, (e) O^3P volume mixing ratio, and (f) $\text{O}^3\text{P}/\text{CO}_2$ volume mixing ratio. Thick curves are the means of individual profiles at 40°N from the Mars Climate Database (MCD: Lewis et al., 1999) for average levels of dust-loading and solar activity. Thin curves are minimum and maximum profiles, and gray shading in panels b, c, e and f depicts the distribution density of the individual MCD profiles.

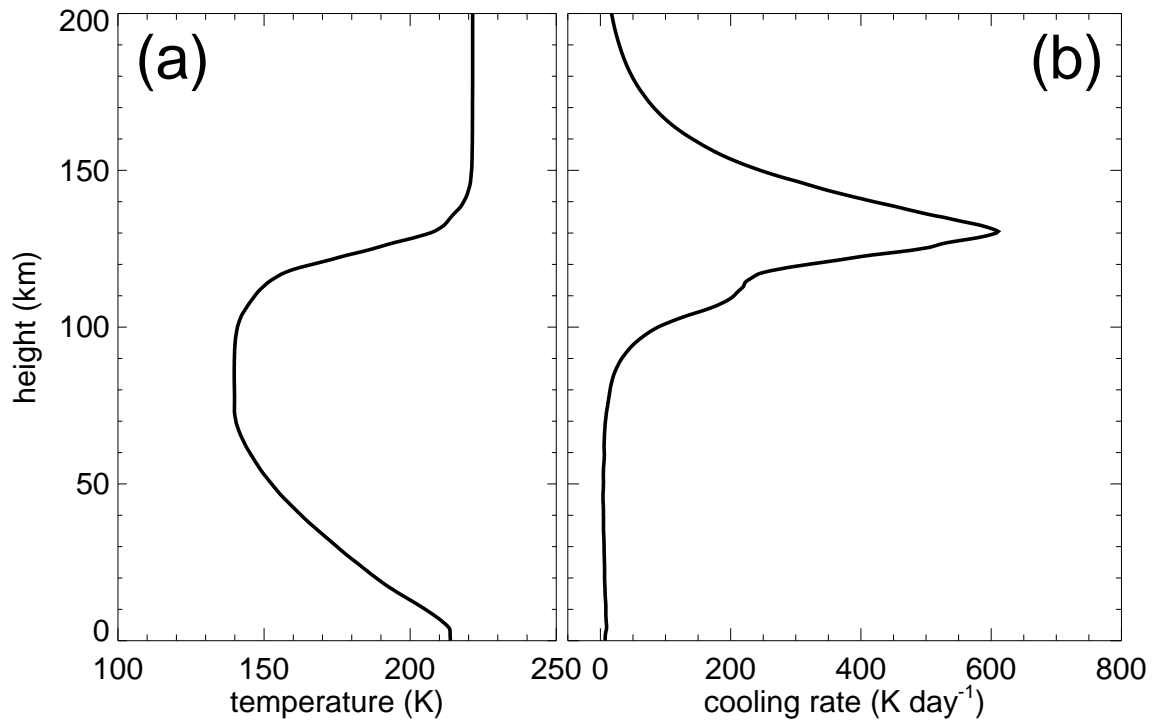


Figure 2: (a) Mean kinetic temperature profile used by López-Valverde et al. (1998) (their Figure 1a); (b) resulting $15 \mu\text{m}$ cooling rates using our Curtis-matrix algorithm and the mean O and CO_2 mixing ratio profiles from Figures 1c and 1e. Rates are quantified here and elsewhere in terms of Earth days: rates in K sol^{-1} are obtained by multiplying the values in (b) by 1.027491.

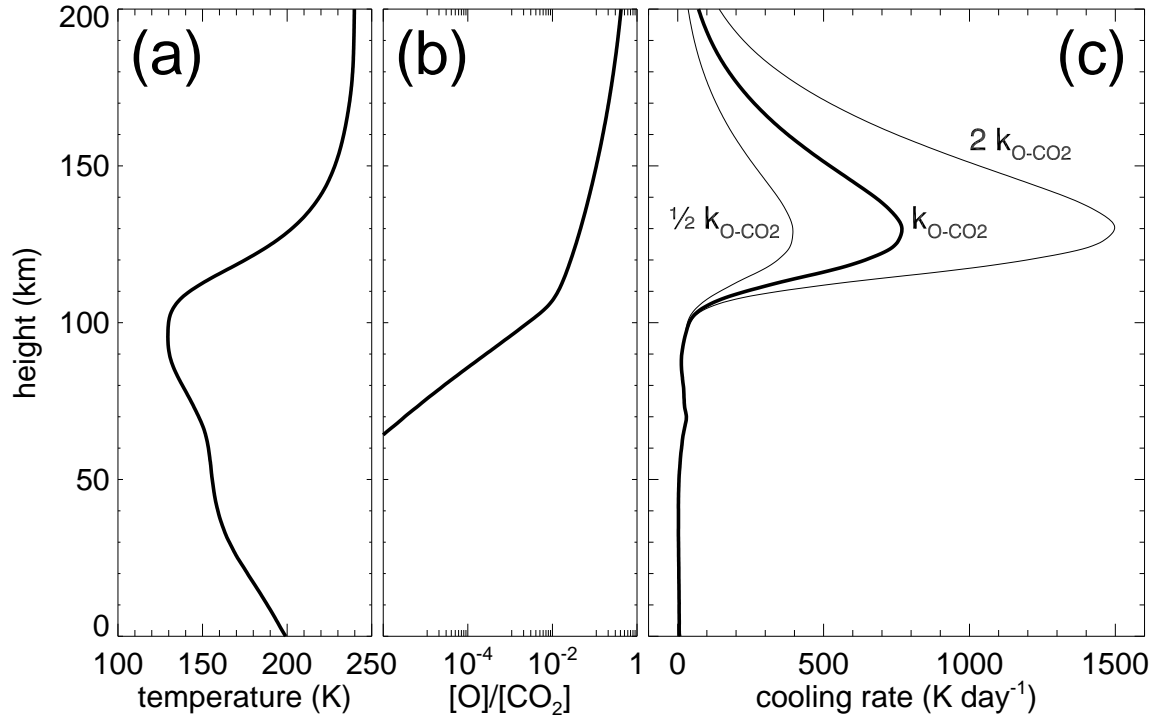


Figure 3: Profiles of mean (a) kinetic temperature and (b) O/CO₂ mixing ratio from Figures 1b and 1f, respectively, which yield in (c) a mean IR cooling rate, plotted with a thick curve, for our prespecified O-CO₂ deactivation rate, k_{O-CO_2} , of $3 \times 10^{-12} \text{ cm s}^{-1}$. Thin curves in (c) show corresponding cooling rates when this k_{O-CO_2} value is doubled and halved.

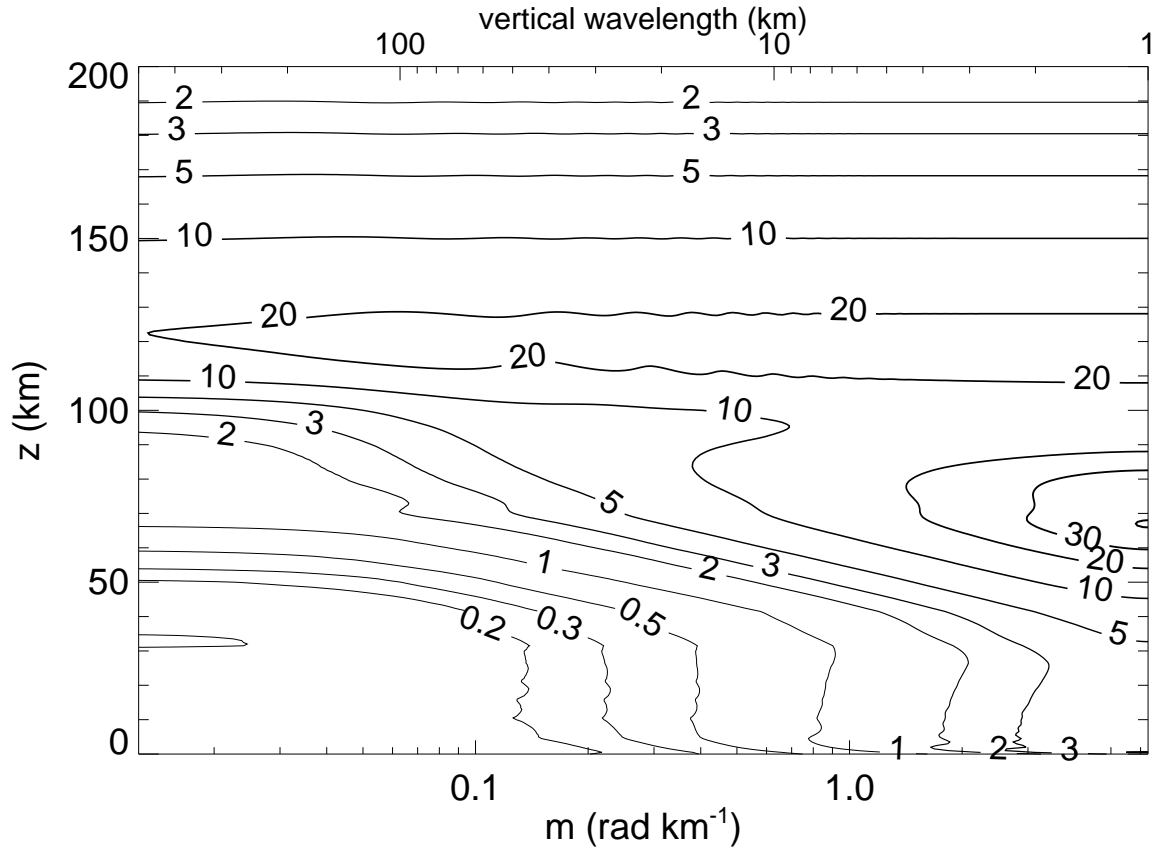


Figure 4: Scale-dependent IR radiative damping rates, $\tau_r^{-1}(z, m)$, (contour labels in days^{-1}) computed for background conditions defined by the mean profiles in Figure 1.

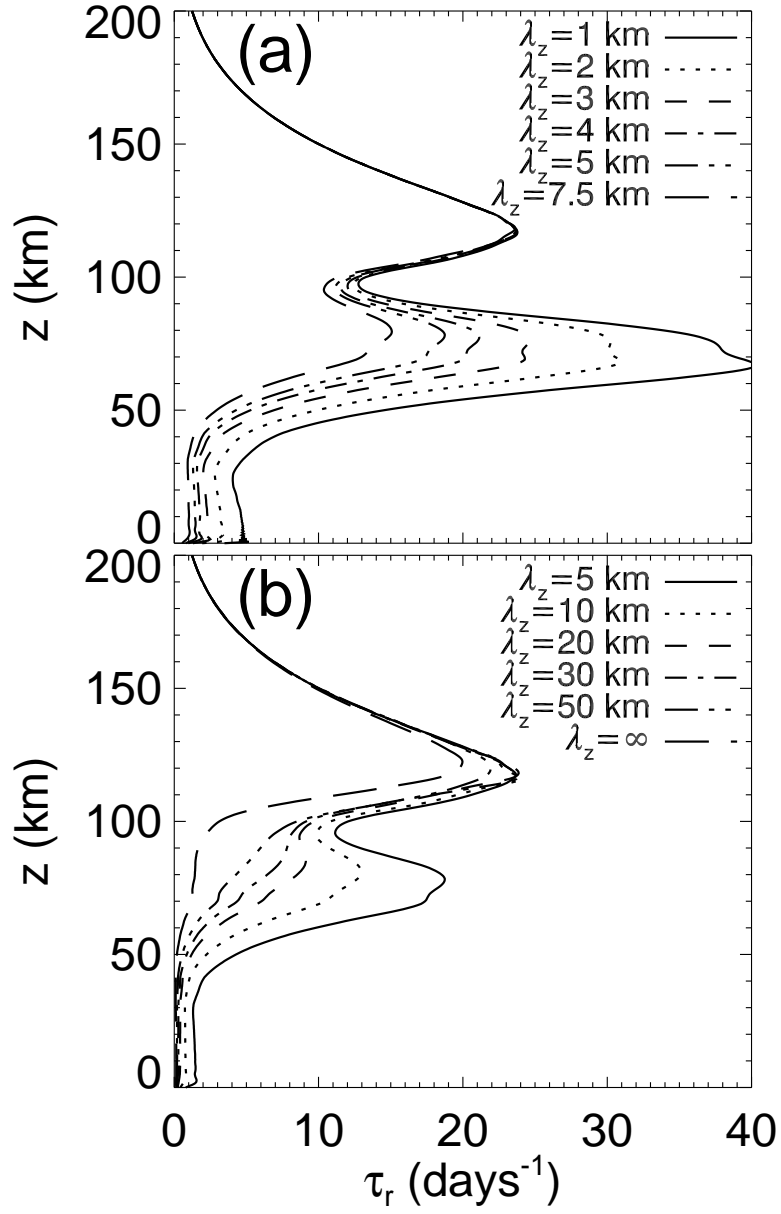


Figure 5: Scale-dependent IR radiative damping rates, $\tau_r^{-1}(z, m)$, plotted as a function of height z for various $\lambda_z = 2\pi/m$ values shown in top right of each panel.

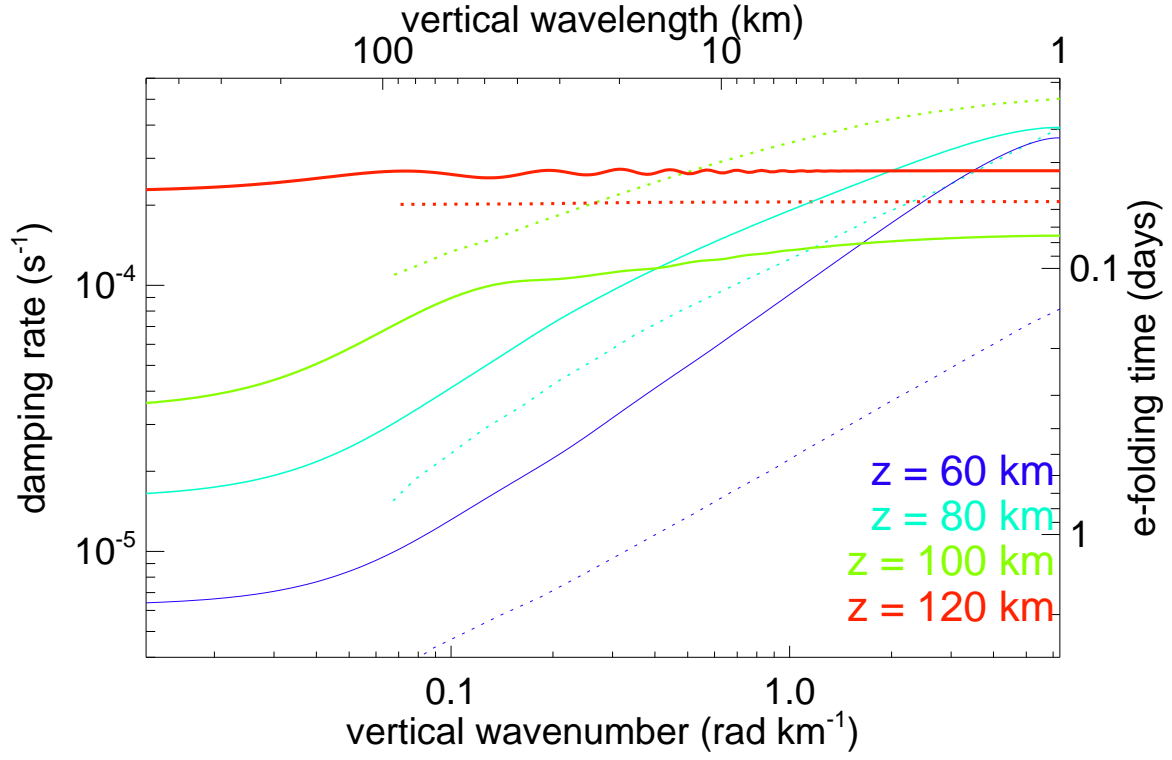


Figure 6: A comparison of IR radiative damping rates, $\tau_r^{-1}(z, m)$, at $z = 60, 80, 100$, and 120 km in the present work (solid curves) and corresponding estimates of Imamura and Ogawa (1995) (dotted curves).

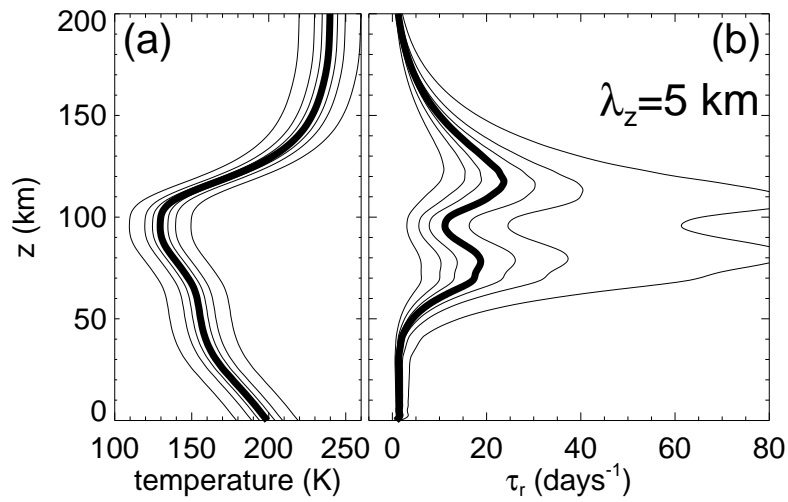


Figure 7: Variation of IR radiative damping rate $\tau_r^{-1}(z, m)$ at $\lambda_z = 2\pi/m = 5$ km as the reference temperature profile in (a) (thick curve) is modified at all heights by -20 K, -10 K, -5 K, $+5$ K, $+10$ K and $+20$ K (thin curves).

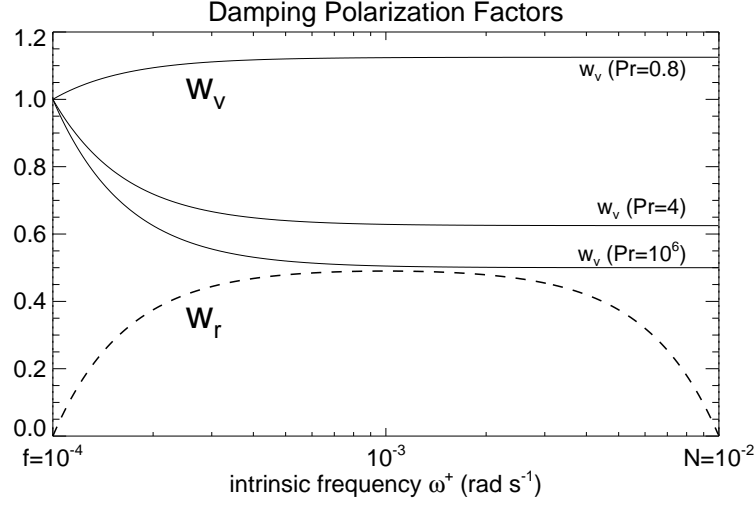


Figure 8: Weighting factors w_r and w_v in (17) and (18) that scale the raw radiative and viscous damping rates τ_r^{-1} and τ_v^{-1} to yield the net rate of damping of gravity-wave amplitudes.

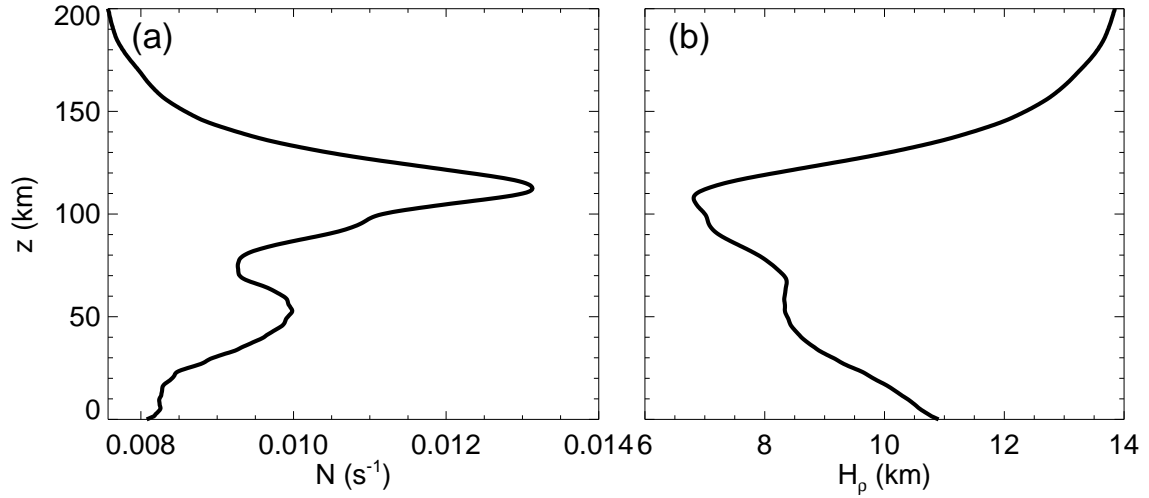


Figure 9: Profiles of mean (a) buoyancy frequency N and (b) density scale height H_ρ , based on the mean background kinetic temperature profile $T_b(z)$ (thick solid curves in Figures 1b and 7a).

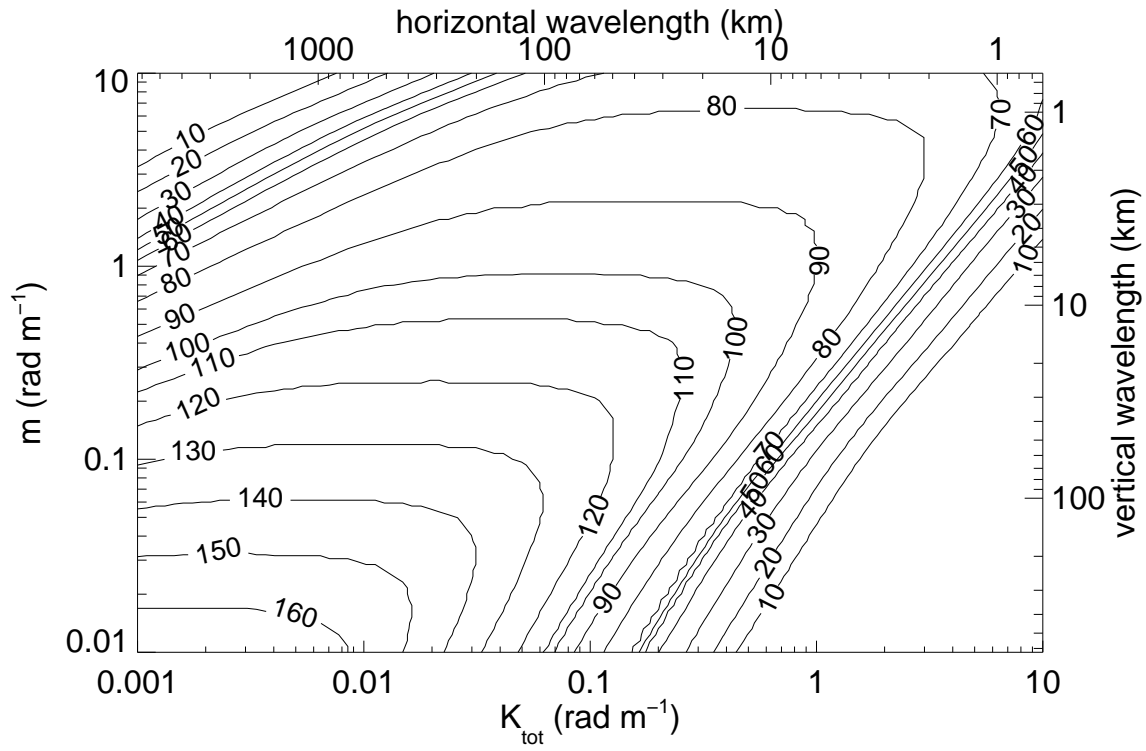


Figure 10: Contours of z_v (labels in km), the altitude above which the local molecular viscous damping of gravity waves, $w_{vm}\tau_{vm}^{-1}$, exceeds the IR radiative damping of the waves, $w_r\tau_r^{-1}$, for gravity waves of the indicated horizontal and vertical wavenumbers.

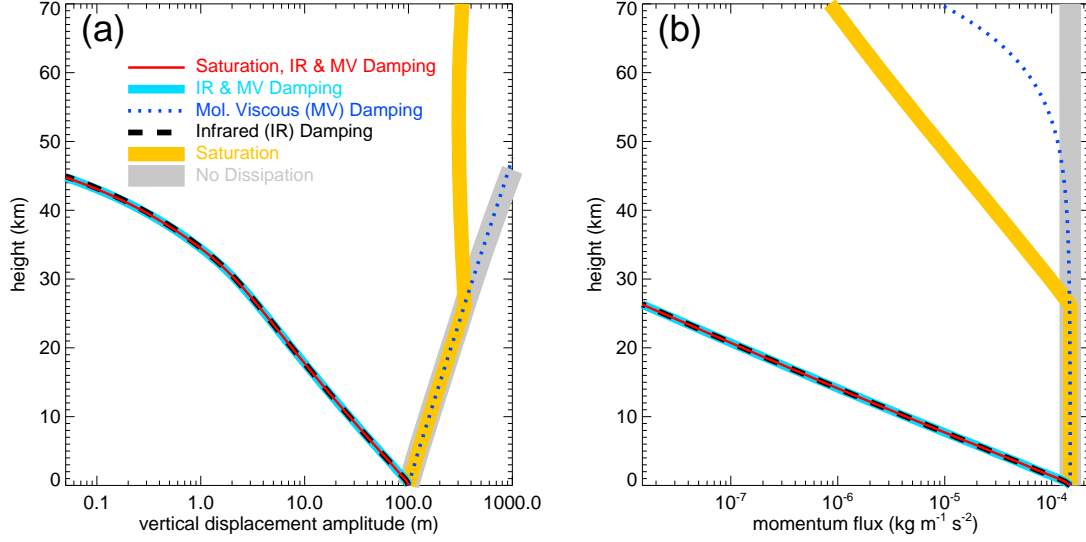


Figure 11: Profiles of (a) peak vertical displacement amplitude $\hat{\zeta}(z)$ and (b) vertical flux of horizontal momentum $F(z)$ for a gravity wave of $c = 3.6 \text{ m s}^{-1}$, $\lambda_z(z_s) = 2\pi/|m(z_s)| = 2.5 \text{ km}$, $\lambda_h = 2\pi/K_{tot} = 100 \text{ km}$, and $\hat{\zeta}(z_s) = 100 \text{ m}$. The curves show solutions for different types of wave damping: no damping (gray solid curves), wave breaking/saturation only (gold solid curves), molecular viscous damping only (blue dotted curves), IR radiative damping only (black dashed curves), molecular viscous and IR radiative damping (aqua solid curves), and all three damping processes (wave breaking/saturation, molecular viscous damping and IR radiative damping: red solid curves).

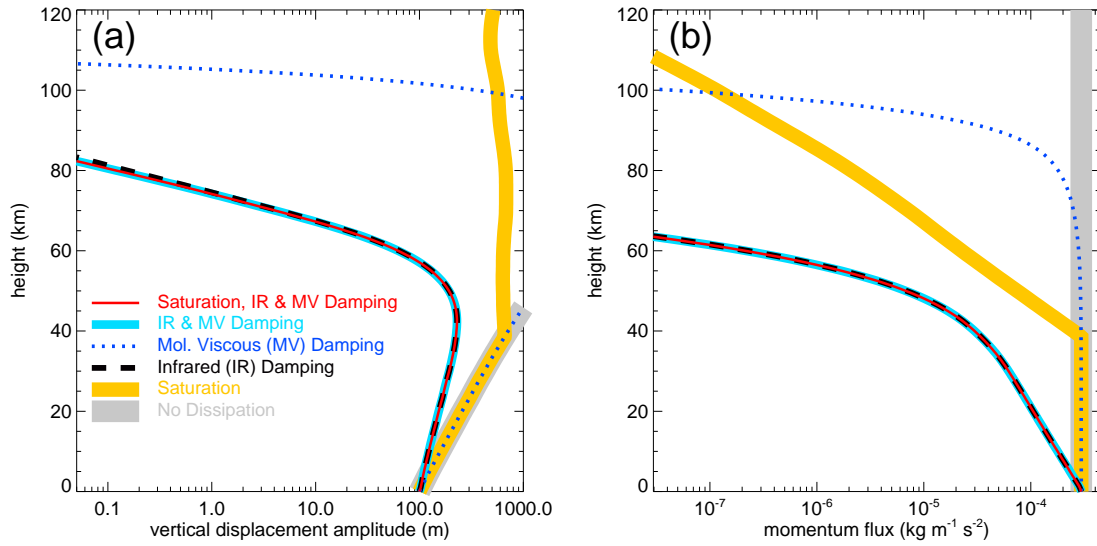


Figure 12: As for Figure 11 but for a gravity wave of $c = 6.6 \text{ m s}^{-1}$ and $\lambda_z(z_s) = 2\pi/|m(z_s)| = 5 \text{ km}$.

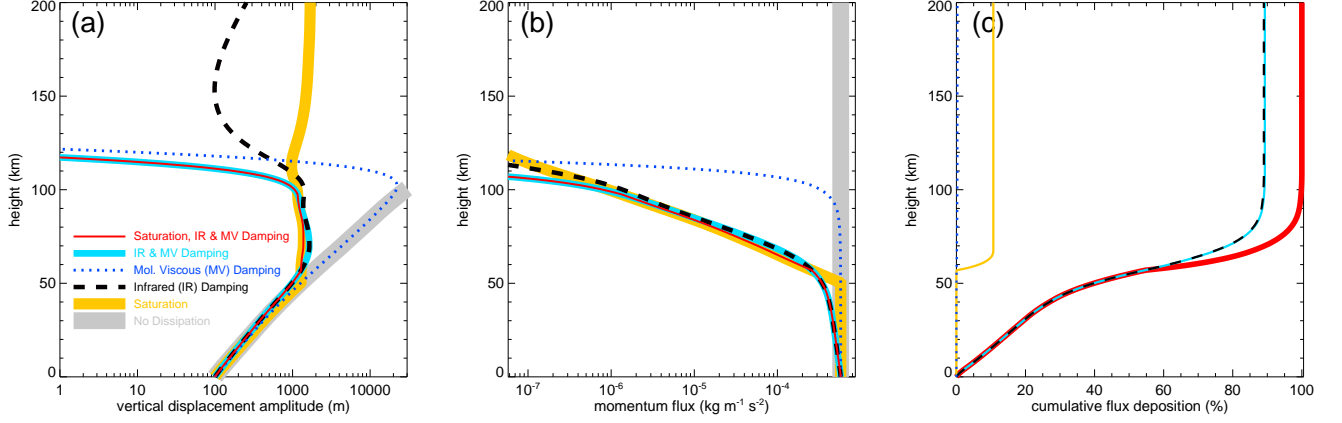


Figure 13: Panels (a) and (b) follow the same presentation as Figure 11 but for a gravity wave of $c = 12.9 \text{ m s}^{-1}$ and $\lambda_z(z_s) = 2\pi/|m(z_s)| = 10 \text{ km}$. The red curve in (c) plots the cumulative deposition of momentum flux $F(z)$, expressed as a percentage of the original source-level flux, for the simulation with all three dissipation processes activated (red curves in panels a and b). Remaining curves in (c) show the contributions to this cumulative flux deposition percentage from breaking/saturation (gold solid curve), IR radiative damping (black dashed curve), molecular viscous damping (blue dotted curve), and combined molecular viscous and IR radiative damping (aqua solid curve).

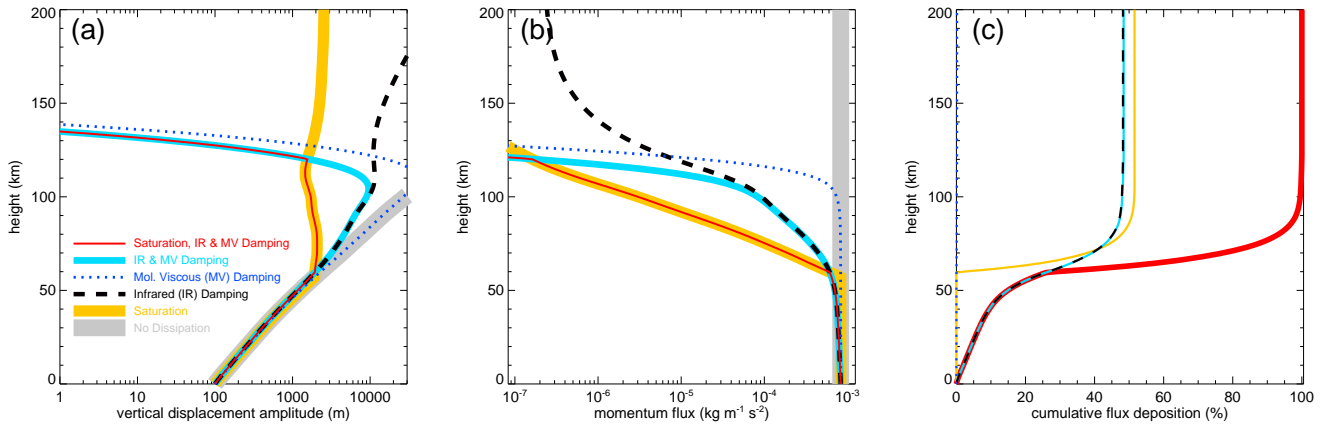


Figure 14: As for Figure 13 but for a gravity wave of $c = 19.0 \text{ m s}^{-1}$ and $\lambda_z(z_s) = 2\pi/|m(z_s)| = 15 \text{ km}$.

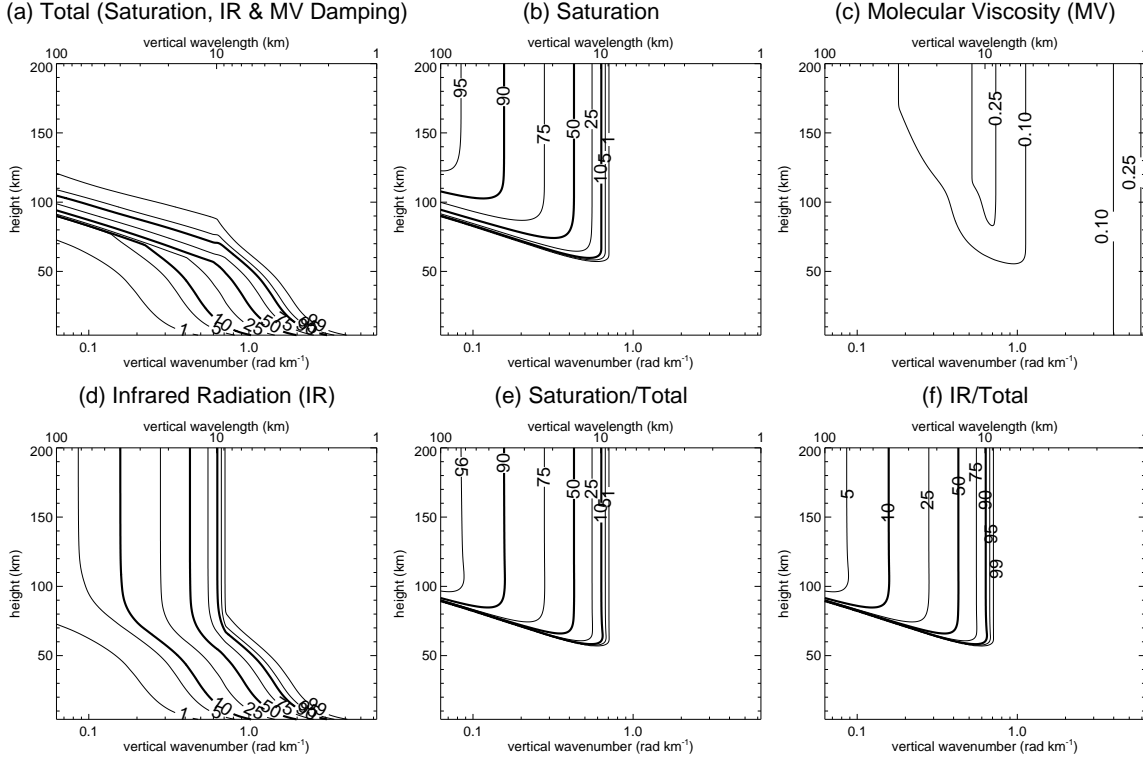


Figure 15: Cumulative percentages of dissipated gravity-wave momentum flux (0% = no dissipation, 100% = total dissipation) as a function of height z and source-level vertical wavenumber $|m(z_s)|$, for model-simulated gravity waves of $K_{tot} = 2\pi(100 \text{ km})^{-1}$ and $\hat{\zeta}(z_s) = 100 \text{ m}$ with all damping mechanisms activated. Plots show (a) the total percentage of dissipated flux, and then contributions to this total from (b) breaking/saturation, (c) molecular viscous damping and (d) IR radiative damping. Remaining panels show the percentage contribution to the local total in (a) from (e) breaking/saturation and (f) IR radiative damping, the latter showing the dominant (i.e. >99%) role of IR radiative damping in gravity-wave momentum flux deposition for all waves at $z \lesssim 50\text{--}80 \text{ km}$ and for waves of $\lambda_z(z_s) \lesssim 10 \text{ km}$ at all altitudes.

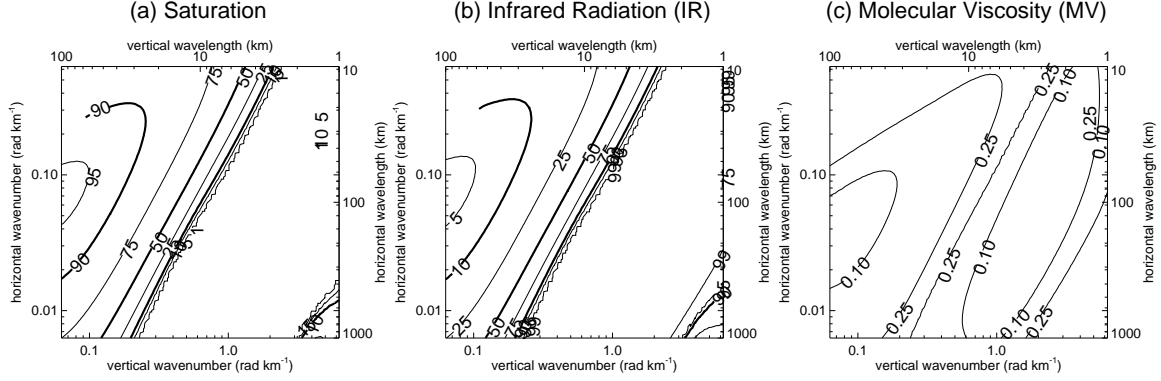


Figure 16: “Top-of-the-atmosphere” contributions to gravity-wave momentum flux dissipation of simulated gravity waves as a function of source-level vertical wavenumber $|m(z_s)|$ and horizontal wavenumber K_{tot} at $z = 200$ km, where close to 100% of each wave’s momentum flux has been dissipated. Contour labels are percentages, due to (a) breaking/saturation, (b) IR radiative damping and (c) molecular viscous damping.

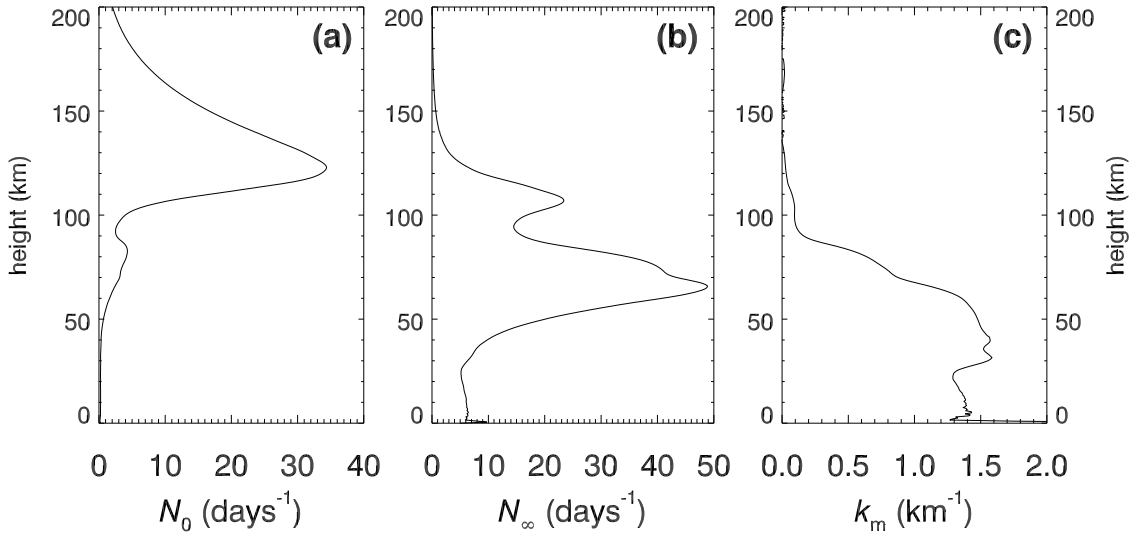


Figure 17: (a) $N_0(z)$, (b) $N_\infty(z)$ and (c) $k_m(z)$ derived by fitting (A.1) to the $\tau_r^{-1}(z, m)$ estimates.

Appendix A. Least Squares Fits to $\tau_r^{-1}(z, m)$

We have fitted the scale-dependent IR radiative damping rates in Figure 4 to various functions to facilitate their efficient numerical implementation in gravity-wave models and parameterizations. Following Zhu (1993), we first performed a nonlinear fit of the rates at each height z to the analytical function

$$\tau_{r_{fit}}^{-1}(z, m) = N_0(z) + N_\infty(z) \left\{ 1 - \frac{\tan^{-1} [m/k_m(z)]}{m/k_m(z)} \right\}. \quad (\text{A.1})$$

This equation fits the rates as the sum of a cooling-to-space term, $N_0(z)$, plus a layer exchange term based on the analytical solution of Spiegel (1957) for an infinite homogeneous atmosphere (Goody and Yung, 1989). By analogy to the Spiegel (1957) solution, $k_m(z)$ is the mean absorption coefficient and $N_0(z) + N_\infty(z)$ is the damping rate in the transparent limit. Using (A.1), scale-dependent radiative damping rates for the reference temperature profile and constituent mixing ratio profiles are now conveniently parameterized in terms of a lookup table of reference profiles of $N_0(z)$, $N_\infty(z)$, and $k_m(z)$, which are plotted in Figure 17. This fit has the advantage that it is well-behaved and relaxes to physically plausible constant values at $m = 2\pi/\lambda_z$ values outside the $\lambda_z = 1\text{-}500$ km range where we computed raw rates from our Curtis matrix calculations.

A drawback is that close fits to the original data do not occur at every height and wavenumber using this function. We obtained much closer fits using the third-order logarithmic polynomial fit

$$\tau_{r_{fit}}^{-1}(z, m) = \exp \left[a(z) + b(z)\psi + c(z)\psi^2 + d(z)\psi^3 \right], \quad (\text{A.2})$$

$$\psi = \log m - \log 2\pi(500 \text{ km})^{-1}. \quad (\text{A.3})$$

While this fit has the advantage of yielding a much more accurate fit at all heights over our 1-500 km vertical wavelength range, it is poorly behaved outside of this wavelength range and thus cannot be used at wavelengths shorter than 1 km or longer than 500 km, which is not a serious drawback since in this case the rate at the limiting boundary wavenumber is imposed.

Lookup tables containing coefficients of both fits on the height grid z_k are provided online as supplementary material, in the form of two text files designed to be used as data files for a computer subroutine that reads in and then uses these coefficients to compute damping rates. These lookup tables also store the background temperature profile $T_b(z_k)$, so that fitted rates can be scaled to any local temperature profile $T(z)$ using (11) and (12).

Appendix B. Anelastic Gravity Wave Model

Our one-dimensional model of gravity-wave evolution with height is based on the anelastic gravity wave equations of Marks and Eckermann (1995). For use on our height grid z_k , we set the ray time step Δt to $\Delta z/c_{gz}$, where $\Delta z = 0.5$ km is our grid resolution, and

$$c_{gz} = \frac{-\omega^+ m \left(1 - \frac{f^2}{\omega^{+2}}\right)}{k^2 + l^2 + m^2 + \alpha^2}, \quad (\text{B.1})$$

is the wave's vertical group velocity. We next define a complex vertical wavenumber $M = m + im_i$, such that

$$m_i = \frac{1}{\tau_w c_{gz}}, \quad (\text{B.2})$$

such that momentum flux varies with height above its source altitude $z > z_s$ as

$$\mathbf{F}(z) = \mathbf{F}(z_s) \mathcal{S}^2(z) \exp \left[-2 \int_{z_s}^z m_i(z') dz' \right]. \quad (\text{B.3})$$

$\mathcal{S}^2(z)$ is a scaling factor that accounts for the accumulated loss of momentum flux due to wave breaking ($0 \leq \mathcal{S}(z) \leq 1$), and is described below, while $\exp[-2 \int_{z_s}^z m_i(z') dz']$ is the time-integrated loss of momentum flux along the ray path due to radiative and viscous damping. In the absence of these dissipative processes, both terms equal unity, whereupon $\mathbf{F}(z) = \mathbf{F}(z_s)$ and $\partial \mathbf{F} / \partial z = 0$.

We initialize momentum flux at the source altitude z_s by specifying the wave's peak vertical displacement amplitude $\hat{\zeta}(z_s)$, which is then converted into a corresponding action density,

$$A = \frac{1}{4} \frac{\rho_b(z) P(z) \hat{\zeta}_s^2}{\omega^+}, \quad (\text{B.4})$$

and momentum flux, \mathbf{F} , via (14), where the polarization factor

$$P(z) = \frac{\left(1 + \frac{f^2}{\omega^{+2}}\right) \left(1 - \frac{\omega^{+2}}{N^2}\right)^2}{\left(1 + \frac{\omega^{+2}}{N^2}\right) \left(1 - \frac{f^2}{\omega^{+2}}\right)} + \left(1 - \frac{\omega^{+2}}{N^2}\right) \quad (\text{B.5})$$

(an equivalent derivation in terms of horizontal velocity amplitude is given in Appendix B of Marks and Eckermann, 1995). Eqs. (14), (B.1), (B.4) and (B.5) imply that the wave amplitude varies with altitude as

$$\hat{\zeta}(z) = \hat{\zeta}(z_s) \left[\frac{\mathcal{S}^2(z) P(z_s) \rho_b(z_s) \omega^+(z) c_{gz}(z_s)}{\mathcal{S}^2(z_s) P(z) \rho_b(z) \omega^+(z_s) c_{gz}(z)} \right]^{1/2} \exp \left[- \int_{z_s}^z m_i(z') dz' \right]. \quad (\text{B.6})$$

As the wave propagates upwards, at each height z_k we check whether wave amplitudes exceed the local threshold amplitude for wave breaking $\hat{\zeta}_{sat}$:

$$\hat{\zeta}(z) > \hat{\zeta}_{sat} = \frac{a}{|m|}, \quad (\text{B.7})$$

where the dimensionless wave-breaking amplitude a is given by eqs. (33) and (34) of Fritts and Rastogi (1985), such that $0 < a < 1$ for $f^2/\omega^{+2} \neq 0$ due to wave-induced dynamical (shear) instabilities, and $a \rightarrow 1$ for $\omega^{+2} \gg f^2$ due to onset of wave-induced convective instabilities. We adopt the standard linear saturation hypothesis used in most parameterizations, in which the wave sheds sufficient momentum flux to reduce the wave amplitude to the threshold for instability ($\hat{\zeta} = \hat{\zeta}_{sat}$), which is achieved by setting

$$S(z) = \min \left[1, \frac{\hat{\zeta}_{sat}(z)}{\hat{\zeta}(z)} \right], \quad (\text{B.8})$$

$$\mathcal{S}(z_k) = \prod_{i=0}^k S(z_i). \quad (\text{B.9})$$